CONNECTIVE TISSUE POLARITY

Optical Second-harmonic Microscopy, Crossed-beam Summation, and Small-angle Scattering in Rat-tail Tendon

ISAAC FREUND,* MOSHE DEUTSCH,* AND AARON SPRECHER‡
*Department of Physics and ‡Department of Computer Sciences, Bar-Ilan University, Ramat-Gan 52100, Israel

ABSTRACT Connective tissue polarity has remained an intractable enigma for over two decades. We present new data on optical second harmonic generation in native, wet, rat-tail tendon. Scanning second-harmonic microscopy has revealed, for the first time, the existence of a discrete network of fine, polar, filamenteous or columnar, structures, and, also, the presence of strongly polar surface, or near-surface patches. The thickness of these features was probed via crossed-beam optical frequency summation and the polar material is estimated to occupy a few percent of the tendon volume. The three-dimensional spatial distribution of filaments was studied with the aid of small-angle second-harmonic scattering, and the filaments were found to permeate the tendon cross-section in an apparently random fashion. These latter measurements also revealed that essentially all polar filaments had the same directionality. Concommitant studies of the polar collagen fibrils that comprise the bulk of tendon were in full accord with prior electron microscope results that had demonstrated that the directionality of these fibrils varies up/down in a purely random fashion, and thus cannot yield a net macroscopic polarity. Quantitative analysis of the second-harmonic data yields the conclusion that the observed polar structures cannot be simply local regions containing some accidental net excess of similarly oriented fibrils. The analytical expressions used in the analysis of the data obtained for this complex tissue were supported by extensive, realistic computer simulations. The discovery that the polarity of rat-tail tendon, and possibly other forms of connective tissue, resides in discrete structures, some of which are located near the tendon surface, should permit the ready isolation of polar-rich material for further study by a variety of techniques.

INTRODUCTION

Some 20-odd years ago Fukada and Yasuda (1) discovered that dried Achilles tendon exhibited a significant piezoelectric effect. The primary requirement for piezoelectricity is the absence of a center of inversion (2), a requirement met by all helical molecules, so that most fibrous biological systems can and do display this phenomenon (3–5). Whether or not such piezoelectricity is biologically functional remains a matter of speculation, in part because piezoelectricity is an inevitable by-product of biomolecular structures rather than being due to some specifically ordered arrangement. Among the piezoelectric coefficients of tendon, Fukada and Yasuda (1) found some that suggested that this tissue has an overall macroscopic polarity. Such a polarity can only arise from specific molecular arrangements maintained over macroscopic distances, and this does suggest the possibility of biological functionality. The magnitude of the uniquely polar coefficient d_{33} was very small, however, being only a few percent of the large coefficient d_{14} related to the helicity of collagen, which is the major component of tendon. The smallness of the polar coefficient tends to argue against biological functionality, and also raises problems of interpretation, since decomposition of the piezoelectric response into large nonpolar and small polar coefficients assumes (*a*) that the sample may be treated in the same way as a uniform crystal, and (*b*) that an unambiguous distinction can be made between tensile and shear stresses (3). These assumptions are, of course, difficult to defend a-priori for an inhomogeneous, multicomponent, mechanically and possibly electrically complex system, such as dried tendon.

Shortly after the work of Fukada and Yasuda, Lang (6) demonstrated that dried tendon exhibited a pyroelectric effect. Since pyroelectricity is the classic test for polarity in crystals (2), Lang's results appeared to confirm the piezoelectric findings and opened up a broad range of inquiry into pyroelectricity in an amazingly wide variety of (dried) biological systems (7, 8). Once again, however, the observed pyroelectric signals were very small, being two to three orders of magnitude less than is usual for strongly polar crystals. Although there are no large "nonpolar" pyroelectric coefficients that could cause confusion in the data analysis, the smallness of the effect not only argues against biological functionality, but also leads to a degree of uncertainty in interpretation, since the pyroelectric effect can be susceptible to artifacts arising from spatial inhomogeneities (2). Indeed, subsequent work on dried

BIOPHYS. J. © Biophysical Society · 0006–3495/86/10/693/20 $1.00
Volume 50 October 1986 693–712

bovine tendon (9) showed large irreversible "pyroelectric" currents at temperatures much above the melting point of the sample, currents that exceeded lower temperature values by several orders of magnitude, and which could not possibly be related to the pyroelectric effect of an ordered, polar system.

Since there did not appear to be any sound biological rationale for these small electrical phenomena and the interpretation that they were related to some sort of connective tissue polarity, a reasonable suspicion appeared to be (10) that perhaps the drying process reduced the system symmetry and thereby gave rise to various small effects unrelated to the structure and function of the native tissue. Electrical measurements are, of course, very difficult to perform in native wet tissue due to its high ionic conductivity. Anderson and Eriksson (11) attempted to circumvent this difficulty by searching for a fast transient piezoelectric effect in wet tendon, but found their sensitivity ultimately limited by streaming potentials, and no positive effect was observed. This important study did, however, bring to the forefront the problem of ionic charge separation (such as might be induced during drying) in electrical measurements of biological samples.

More recently, using optical second-harmonic generation (SHG), we were able to confirm the existence of a net macroscopic polar ordering in native rat-tail tendon (RTT) continuously maintained in physiological phosphate buffer (12, 13). Since a structure displaying macroscopic polar order should also exhibit both piezo- and pyroelectricity, our results on the native, wet tissue confirmed the pioneering findings of both Fukada and Yasuda (1), and of Lang (6). Our SHG data appear to be unambiguous, since the only second harmonic (SH) coefficients observed were those appropriate to a polar system. Also, our method is structural, rather than phenomenological, so we were able to avoid many of the difficulties of interpretation and inference that had plagued earlier studies. Here too, however, the observed SH coefficients were small, an order of magnitude less than is usual for strongly polar crystals. Accordingly, doubts regarding functionality, and, in light of the newness of the method, perhaps even of interpretation, still persisted. And so, more than two decades after its initial discovery, one still did not know if connective tissue polarity was meaningful in any biological sense, while nothing at all was known about its structural basis.

SURVEY OF RESULTS

Because of the complexity of the material, we briefly describe here in general form our major results and conclusions, deferring to later sections details on theory, methods, instrumentation, specific data, and their analysis.

RESULTS

Our primary finding is that the polarity of RTT resides in two types of specific structures: (*a*) a fine network of polar, filament-like objects that permeate the tendon volume, and (*b*) a small number of strongly polar surface, or near-surface patches, which may possibly consist of dense collections of unresolved filaments. These structures were visualized by scanning SH microscopy (14–17) with supplemental information being obtained from crossed-beam SHG and small-angle SH scattering. The polar structures could not be observed by either bright-field, dark-field, polarization, or phase-contrast microscopy. We estimate that a typical polar filament has a diameter of order 10 μm, and that the polar material occupies a few percent of the tendon volume. We also determined that most, if not all, polar filaments have the same directionality (sign). Finally, we found no major qualitative differences between tail tendons from animals 1–6 months of age.

DISCUSSION

What significance should be attached to these findings? The answer lies in our current knowledge of the structure of tendon. Rat-tail tendon, widely studied as a classic representative of regular connective tissue (10), is composed principally of a dense parallel array of polar collagen fibrils which range in diameter from ~0.02–0.5 μm. The number of fibrils with a given diameter varies, approximately, inversely with the diameter. The directionality of the fibrils may be determined from a study of assymetric banding patterns under the electron microscope, and it has long been known that this directionality varies randomly throughout the tendon. Parry and Craig (18) have performed an extensive quantitative study and concluded that both locally and globally the number of "up" fibrils equals the number of "down" fibrils to within the few percent uncertainty of their counting statistics. The implication here is that the directionality of the fibril is biologically indifferent, but the corollary of this is that there need be no special mechanism for ensuring true directional randomness. This, in turn, immediately raises the possibility that the structures we observe may be simply regions containing some accidental net excess of, say, up fibrils. Two lines of evidence point against this. (*a*) The fact that most, if not all, filaments are of the same sign implies that the directionality is mechanistically determined. (*b*) Intensity considerations indicate that if composed of collagen fibrils, the filaments must consist of arrays in which essentially all fibrils have the same directionality. This, too, implies a deterministic mechanism. In later sections we will present evidence that suggests, although does not prove, that the filaments and patches are probably not composed of collagen fibrils. But such a conclusion immediately raises the question of why not? If polar structures are required biologically, why should these not be fabricated from the readily available collagen fibrils? In answer to this we will argue that the structure of collagen is such that its dipole moment, and hence the electric moment of the fibril, is relatively small, so that the fibrils do not constitute a particularly useful source of polar material.

Are the filaments and surface patches really strongly polar? SHG does not, in fact, measure electric moments, and so cannot give direct information about the strength of the polarity. Our observation that the polar material occupies only a few percent of the tendon volume provides a ready explanation for the smallness of the observed piezo- and pyroelectric coefficients, since these are simply average values for large volumes. But this, in turn, suggests that the filaments and patches have piezo- and pyroelectric coefficients comparable to those of strongly polar crystals, and thus, are themselves strongly polar. Then, there must be some defined biological mechanism for generating this strongly polar material, so one is led to conclude that the polarity may well be functional. What this function might be, and what might be the consequences of disturbing or misaligning the polarity during say, surgery, are at present only matters of speculation. It should prove possible, however, to isolate strongly polar regions of tissue for further study by a variety of techniques, and thus ultimately to resolve the 20-yr-old enigma of connective tissue polarity.

SECOND HARMONIC GENERATION

There are two main approaches to treating SHG theoretically. One involves direct solution of Maxwell's equations for wave propagation in a medium whose response is nonlinear. This is most useful for simple, regular sample shapes, and has been fully developed by Bloembergen and coworkers (19, 20). We will make only limited use of this method here. A second, more useful approach for our purposes, is to sum the second harmonic fields radiated by the oscillating nonlinear polarizations induced in each elementary unit by the incident laser field. This method, familiar from both light and x-ray scattering, has also been briefly discussed by Bloembergen and Pershan (19), and developed more fully in a form appropriate to our needs in a seminal paper by Bersohn and co-workers (21). This second approach easily handles SHG by objects of arbitrary shape, but with one proviso: that these be embedded in an index-matching medium, so that the phase differences of the various waves arriving at the detector plane depend only on the spatial separation and orientation of the elementary radiators. This condition is very well met in our case since, as mentioned, the SH emitting structures we study are so closely index-matched to the surrounding tissue that they are invisible even under the phase-contrast microscope.

Polarization Dependence

Our starting point is the usual premise that the incident laser field, $\mathbf{E}^{(1)}(\mathbf{r})$ at the frequency ω_1, induces a second-order polarization at the frequency $\omega_2 = 2\omega_1$, given by (22)

$$P_i^{(2)}(\mathbf{r}) = \sum_{j=1}^{3}\sum_{k=1}^{3}\beta_{ijk}(\mathbf{r})E_j^{(1)}(\mathbf{r})E_k^{(1)}(\mathbf{r}). \tag{1}$$

Here the subscripts ijk refer to an orthogonal coordinate system, and the "hyperpolarizability" β is assumed to vary with $\mathbf{r}$. Eq. 1 simplifies considerably in many instances (23), including our case in which all the structures we observe are found to conform to C_∞ symmetry. Taking the Z axis as the polar symmetry axis, the Y axis as the direction of propagation of the laser, and the X axis perpendicular to the Y-Z plane, Eq. 1 is reduced by consideration of both spatial and Kleinman (24) symmetry to

$$P_Z^{(2)}(\mathbf{r}) = \beta_{ZZZ}(\mathbf{r})[E_Z^{(1)}(\mathbf{r})]^2 + \beta_{ZXX}(\mathbf{r})[E_X^{(1)}(\mathbf{r})]^2, \tag{2a}$$

$$P_X^{(2)}(\mathbf{r}) = 2\beta_{ZXX}(\mathbf{r})E_X^{(1)}(\mathbf{r})E_Z^{(1)}(\mathbf{r}). \tag{2b}$$

Our measurements are, for the most part, relative ones, so we usually only concern ourselves with the ratio

$$\rho \equiv \beta_{ZZZ}/\beta_{ZXX}. \tag{2c}$$

This ratio is structurally sensitive, and can be used to distinguish between differing molecular structures and arrangements.

In our previous work (12) we showed experimentally that Eqs. 2 accurately describe SHG by both the collagen fibrils and the polar tendon as a whole. Since at that time we had not yet resolved the polar filaments or the surface patches, we consider it worthwhile to verify here Eqs. 2 specifically for each of these structures. As was done previously, we vary the angle, α, that $E^{(1)}$ makes with the Z axis, and measure the relative SH intensity passed by an analyzer oriented either parallel, $I_Z^{(2)}(\alpha)$, or perpendicular, $I_X^{(2)}(\alpha)$, to the long tendon axis, the Z axis. From Eqs. 2 we obtain (with β_{ZXX} set equal to 1)

$$I_Z^{(2)}(\alpha) = [\rho\cos^2\alpha + \sin^2\alpha]^2, \tag{3a}$$

$$I_X^{(2)}(\alpha) = [\sin 2\alpha]^2. \tag{3b}$$

In the absence of the analyzer, of course, the SH intensity $I^{(2)}(\alpha)$ is simply the sum of Eqs. 3a and 3b. A measurement of $I^{(2)}(\alpha)$ is particularly useful in that it establishes a-priori the long tendon axis as the system symmetry axis. In Fig. 1 we display both calculated (Eqs. 3) and measured data for a surface patch; the data for polar filaments were very similar and so these are not shown. Both data sets agree well with calculation and yield $\rho \simeq 1.8$. This is significantly different from the value of $\rho = 1.3$ measured for the collagen fibril (12), and suggests the possibility that the polar structure may not be composed of fibrils. This conclusion is not definitive, however, since, as discussed previously (25), the apparent value of ρ can be affected to some extent by a number of factors that are difficult to control. We have found that the spatial variation of $\beta_{ZZZ}(\mathbf{r})$ and $\beta_{ZXX}(\mathbf{r})$ appears to be the same, consistent with a constant value of ρ for the filaments and surface patches. In the remainder of this work we use Z polarized laser light, and so always measure $\beta_{ZZZ}(\mathbf{r})$. Accordingly, in what follows we drop the subscripts on β.

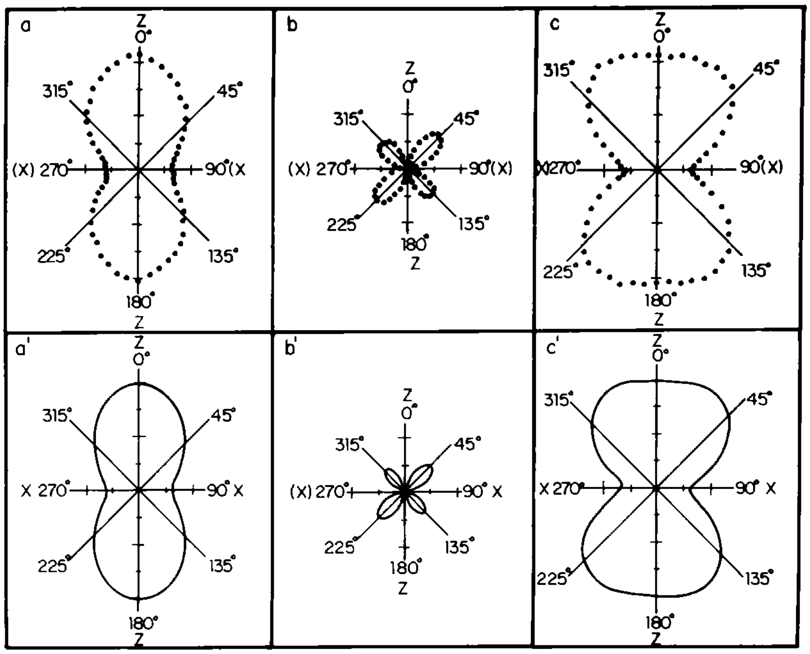

FIGURE 1 Polar plots of SH intensity vs. angle of laser polarization relative to the long tendon axis, the Z axis, for a surface patch. (*a–c*) Measured data. (*a′–c′*) The corresponding calculations (Eq. 3). (*a–a′*) Analyzer parallel to Z axis, $I_Z^{(2)}$ of Eq. 3a. (*b–b′*) Analyzer perpendicular to Z axis, $I_X^{(2)}$ of Eq. 3b (*c–c′*) No analyzer, $I^{(2)}$ of text. $I_X^{(2)}$ is very sensitive to small alignment errors. The marked asymmetry in *b – b′* corresponds to a 2.5° misalignment of the analyzer relative to the tendon axes. These data demonstrate unequivocally that the patch is polar, has C_∞ symmetry, and that the polar axis is along the tendon Z axis.

Angular Dependence

In an SH scattering experiment the measured signal, $S_2(\kappa)$, may be written in terms of what we will call the nonlinear structure factor $G(\kappa)$,

$$S_2(\kappa) = |G(\kappa)|^2, \tag{4a}$$

$$G(\kappa) = \int_{\mathrm{Vol}} \beta(\mathbf{r}) e^{i\kappa\cdot\mathbf{r}} d^3r, \tag{4b}$$

$$\kappa = \mathbf{k}_2 - 2\mathbf{k}_1. \tag{4c}$$

In writing Eq. 4a we have suppressed irrelevent constants. In Eq. 4c $\mathbf{k}_1$ in the wave vector of the incident laser field. This field, via Eqs. 2, drives the nonlinear polarization P_2 with wave vector $2\mathbf{k}_1$. P_2, in turn, radiates the second harmonic, which travels with wave vector $\mathbf{k}_2$. Thus the form of the momentum transfer κ given in Eqs. 4c, which here, as in all scattering experiments, is the relevant variable. As is often the case in light and x-ray scattering, we will also find it useful to use the Wiener-Khinchine theorem (26) and rewrite Eq. 4a as the Fourier transform of the autocorrelation function of $\beta(\mathbf{r})$.

One major difference between SH and normal light scattering is the fact that the sign of β varies with the directionality of the polar unit, being + for, say, up-pointing units, and − for those that point down. This dependence on directionality is unique, and accounts for the special utility of SHG in the study of biomolecular assemblies (27).

As becomes apparent, all the structures we study—the collagen fibrils, the polar filaments, and the surface patches, are greatly elongated along the Z axis, the long tendon axis. Accordingly, Eqs. 4 predict that SH scattering will be nearly confined to the X-Y plane, a prediction we have directly verified experimentally for the different structures. As described previously (12), our apparatus normally contains a long acceptance slit parallel to the Z axis, so that at each scattering angle, θ, we integrate over SH radiation emitted normal to the X-Y plane, the scattering plane. Under these circumstances Eq. 4b reduces to a two-dimensional integral in the X-Y plane, and the required components of κ may be written

$$\kappa_x(\theta) = (4\pi n_2/\lambda_1)\sin\theta, \tag{5a}$$

$$\kappa_y(\theta) = (4\pi n_2/\lambda_1)(\cos\theta - n_1/n_2), \tag{5b}$$

$$\kappa(\theta) = \sqrt{\kappa_x^2 + \kappa_y^2}. \tag{5c}$$

Here $\lambda_1 = 1.064$ μm is the wavelength of our Nd-YAG laser, n_1 is the refractive index at this wavelength, and n_2 is the refractive index at the SH wavelength.

In general $n_2 > n_1$, and this has the important consequence that even for $\theta = 0$, $\kappa(0) = \kappa_y(0)$ is nonzero. The effects of dispersion in n on SHG are often described in terms of a coherence length ℓ_c defined by $\kappa_y(0) \cdot \ell_c = \pi$, or

$$\ell_c = \lambda_1/[4(n_2 - n_1)]. \tag{6}$$

For RTT, ℓ_c has been estimated previously (12) to be ~10 μm.

In later sections we will need an expression for SHG by an ordered plane-parallel slab of thickness T and width W. This is easily obtained from Eqs. 4 (with $\beta = 1$) as

$$S_2(\kappa_x,\kappa_y) = \frac{\sin^2(\kappa_x W/2)}{(\kappa_x/2)^2} \cdot \frac{\sin^2(\kappa_y T/2)}{(\kappa_y/2)^2}. \tag{7}$$

This expression describes a forward-directed nearly collimated SH beam of angular divergence $\lambda_2/n_2 W$, whose intensity oscillates with sample thickness, falling to zero for T equal to even multiples of ℓ_c, and rising to maxima at odd multiples of ℓ_c, so that the maximum useful sample thickness for SHG is $T = \ell_c$. The dependence of Eq. 7 on κ_x suggests that the angular divergence of SHG can be used to measure the transverse dimensions of the polar units, while the dependence on $\kappa_y T$ suggests that the SH intensity can be used to probe the thickness. Of course, as is often the case and as is described in later sections, a considerable degree of both experimental and theoretical elaboration is required to obtain useful results.

SAMPLE PREPARATION

Samples

Tendons were excised from tails of 1–6-mo-old Charles River rats by making two suitably separated transverse cuts and sliding out the cut tendon sections from the distal end. This, and all other procedures, measurements, and refrigerated storage, were normally performed in physiological phosphate buffer. The proximal ends of the tendons were marked by crimping for later reference. In mature rats tail tendons usually occur in groups of typically three loosely intertwined units, which are easily separated without damage. The individual tendons are typically ~0.3 mm in diameter, display the well-known 0.1-mm crimping (28), and are virtually opaque due to intense light scattering; indeed, they look like fine white threads. We could not use thin, cut sections prepared by the usual procedures of fixing, embedding, and slicing, since we found that such sections "burned" in the laser beam, and we, anyway, considered it best to continue to study native, wet tendon, so as to avoid the uncertainties that had clouded early work on dried samples. Frozen sections might have been acceptable, but we could not prepare these with the requisite high optical quality.

Compression

We obtained thin transparent samples, as has been done in previous studies of RTT (12, 29), by compressing tendons held under tension between glass plates to about one-tenth their original thickness. Careful microscope study showed that what happens is principally a simple transverse spreading of the tendon fibers, and that the tendon volume is essentially conserved. We found that the spreading was facilitated by making one of the inner glass surfaces slightly convex, so one window of our sample cell was cut from a half-meter-focal-length plano-convex lens. Near-perfect index-matching and excellent tendon-glass optical contact were usually obtained, and virtually distortion-free passage of optical beams through the cell was readily achieved. When samples of the highest optical quality were required, the buffer bathing the compressed tendon was replaced with distilled water. We believe this results in a slight swelling of the tissue which accounts for the improvement in optical quality. No significant differences in SHG were observed after exchange of the buffer with distilled water. We also noted that the optical quality tended to improve with time, probably as a result of creep. In Fig. 2 we show a low-power dark-field micrograph of a typical sample which illustrates the exceptional degree of transparency obtained.

The compression, of course, distorts the internal tendon structures. In Fig. 3 we display schematically some of the expected distortions. The major result of compression is expected to be a transverse smearing of internal structures with a concomittant decrease in thickness. In our previous work (12) we demonstrated that the level of compression we use does not measurably distort the circular cross-section of the collagen fibril, so that we do not expect extensive disruption of other fibrous components or complete destruction of cellular material. We also note that the polar structures do not appear qualitatively different in tendons stored under refrigeration for several months, so

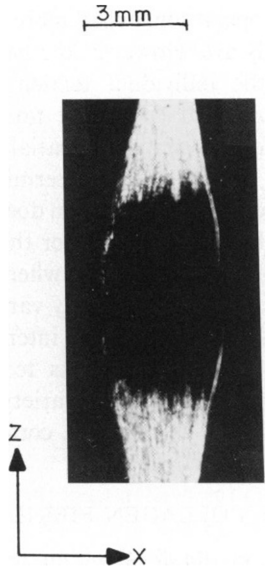

Figure 2 Dark-field low-power photomicrograph of tendon under compression in cell containing one planar and one convex inner surface. The perfect clarity of the central region illustrates the exceptional transparency of the sample. The tendon edges and ends are somewhat less perfectly uniform optically and show strong light scattering under the intense dark-field illumination. In transmitted light the tendon as a whole appears completely transparent. Also shown is the coordinate system used in discussing the tendon properties. The tendon thickness (Y axis) is ~25 μm as estimated from the measured intrinsic birefringence and interference colors observed with crossed and parallel polarizers.

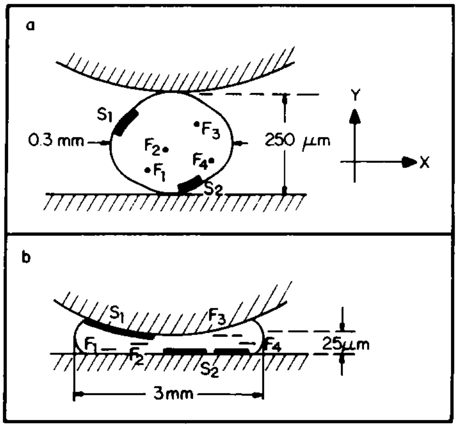

FIGURE 3 Transverse section of tendon between cell windows (*a*) before and (*b*) after compression. Shown schematically are two surface patches (S_1 and S_2) and four polar filaments (F_1–F_4). Compression markedly reduces the thickness of the structures along the *Y* axis, smears them out along the *X* axis, and possibly produces some degree of fragmentation. In our SHG studies the laser propagates along the *Y* axis. The dimensions shown are typical. Note that the overall tendon volume is conserved under compression.

that the constituents of these structures are quite stable. We would expect that the volumes of internal structures be preserved to a large extent, and so could be reconstructed from the volume estimated for the compressed structure. If the intact polar filaments and/or surface patches consist of loose fiber bundles or columns of cells, we could expect that these might sometimes be split, so that the structures we observe might appear somewhat more highly filamented than they actually are. However, the basic relative spatial distribution of the individual tendon structures should generally map uniquely into their final positions in the compressed tendon, so that gross spatial relationships, e.g., surface vs. bulk, should still be determinable. Finally, we have demonstrated that compression does not induce SHG. There are three lines of evidence for this. (*a*) SHG is not more prevalent at the cell center where the compressive forces are greatest. (*b*) Deliberately varying the degree of compression does not cause the SH intensity to vary in any significant way; and (*c*) Attempts to induce SHG via compression (or tension) in a variety of natural and man-made fibers such as cellulose, cotton, polyester, etc., always yielded negative results.

SHG BY COLLAGEN FIBRILS

We review here in detail SHG by collagen fibrils and discuss the impact this has on the interpretation of our other findings.

Angular Dependence

The polar collagen fibril, the major constituent of RTT, is a significant generator of SH radiation. However, all evidence available to date indicates that the polar directions of these fibrils varies up/down in a random fashion (18). SHG by such a random array is incoherent, and may be calculated by summing intensities for each of the fibrils. After normalizing to unity at $\kappa = 0$, this yields (12),

$$S_2(\kappa) = 8[J_1^2(\kappa R) - J_0(\kappa R)J_2(\kappa R)]/(\kappa R)^2. \qquad (8)$$

Here $2R$ is the maximum fibril diameter, the J_n are Bessel functions, and the form of Eq. 8 reflects the known $1/r$ fibril diameter distribution (18). In Fig. 4 we compare measured data with Eq. 8 for a tail tendon from a 3-mo-old animal (12). The agreement is good everywhere, except at zero angle where a sharp peak is observed. In this figure both the width and height of this peak are instrument limited. Under higher (~2 mrad) resolution the apparent peak height is two or more orders of magnitude greater than the fibril background, while its width remains instrument limited. We had in the past interpreted (12) this peak as due to some component of the tendon that exhibits macroscopic, long-range polar order. This component is now known to be the polar filaments and surface patches which, via aperture synthesis, give rise to a forward, sharp, coherent SH peak.

Could the apparently random up/down array of collagen fibrils give rise to a sharp, central peak? Here one must be concerned about the following two possibilities. (*a*) Even conceding purely random up/down statistics, there is, nonetheless, an intrinsic clumping that occurs which leads to significantly sized regions of all up or all down fibrils. A typical example of this, obtained by computer simulation, is shown in Fig. 5. Perhaps these regions are large enough so that they generate a sharp, forward SH peak, while the "filaments" and "patches" are simply illusions arising from the well-known tendency to imagine regular patterns even when only noise is present. We attack this fundamental problem in a simple, straightforward fashion by constructing a highly realistic computer model of tendon and

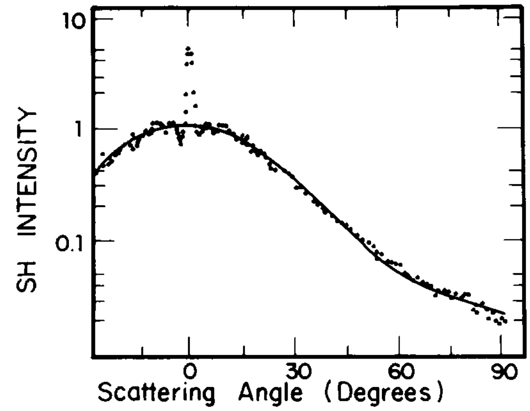

FIGURE 4 SH scattering data from a compressed and hence perfectly transparent tail tendon obtained from a 3-mo-old Charles River rat. The data points were measured using a 1.5° angular resolution and a sample maintained in physiological phosphate buffer. The solid curve is a plot of Eq. 8 using a maximum fibril diameter $2r = 0.53$ μm appropriate to the tendon age and corresponds to incoherent SH scattering by the random up/down array of collagen fibrils. The sharp central peak is due to coherent SH scattering by the polar filaments and patches.

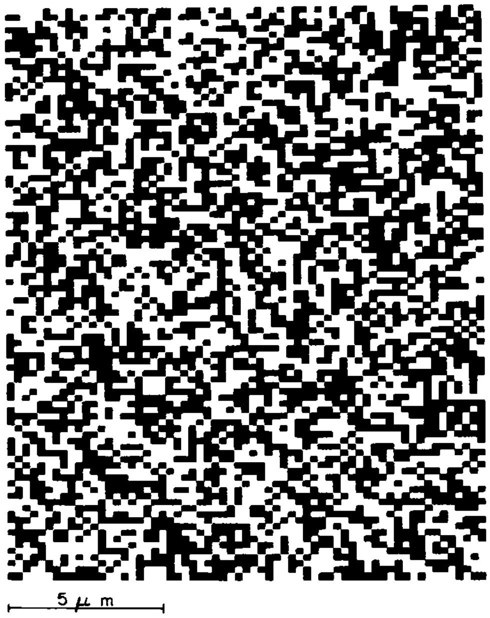

FIGURE 5 Computer simulation of the random up/down array of collagen fibrils. A square lattice is employed with black squares representing fibrils that point, say, up, while white squares represent down-pointing fibrils. The distance scale was chosen to correspond to the ~17/µm² average fibril density of rat-tail tendon. The polarity of each cell was chosen independently and purely randomly with equal weights for up and down. Note the significant degree of clustering of similarly oriented fibrils, which leads to regions of a given polarity that are several microns in length.

study here its SHG. In later sections we will also use this computer model to examine various hypotheses about the nature of the filaments and patches. (*b*) A second cause for concern is the possibility that there might be real, systematic deviations from up/down random statistics, but that these deviations might be meaningless. Biological indifference to fibril directionality need not necessarily lead to true random statistics for the up/down directional distribution. At issue here is the extent of the deviations from randomness: small deviations, even if they are many times those expected statistically, might well not be meaningful; extremely large, systematic deviations, on the other hand, bespeak an underlying cause and are thus likely to be very meaningful indeed. In examining this quantitative question we again find our computer model to be most useful.

Computer Model

As already indicated, only two-dimensional calculations in the X-Y plane are required, so our model of the parallel collagen fibrils consists of several hundred thousand circles randomly distributed, but otherwise nearly close packed, the packing being adjusted so as to match the ~60% coverage of the tendon area measured for the fibrils (18). The circle diameters $2r$ follow the known $1/r$ fibril diameter distribution between the limits $0.018 \leq 2r \leq 0.53$ µm appropriate for 3-mo-old animals (18). These circles make up a sample 25 µm thick along the Y axis, and 1 or more mm wide along the X axis. They are laid down by an algorithm that starts at one end of the sample and zig-zags back and forth parallel to the Y axis, close-packing circles each of whose diameters is randomly chosen in accordance with the $1/r$ distribution. This procedure is entirely "local" and thus minimizes the amount of information that needs to be processed for the placement of each succeeding circle. After completion of the array, all diameters were uniformly shrunk by ~10% so as to yield the correct final packing. This also eliminates circle-circle contacts which is in accordance with electron microscope images of RTT. A typical region of the model is shown in Fig. 6, and may be seen to bear a remarkable resemblance to Fig. 1 of Parry and Craig (18) which displays an electron micrograph of a transverse RTT section.

The SH scattering for this model may be directly calculated from Eqs. 4 as

$$G(\kappa) = \frac{2\pi}{\kappa}\sum_{n} \beta_n r_n J_1(\kappa r_n) e^{i(\kappa_x X_n + \kappa_y Y_n)}, \qquad (9)$$

where the sum is over all circles, and r_n is the radius of the nth circle with center at (X_n, Y_n). The directionality (up = +, down = −) of a given fibril is expressed by the sign of β. For a random up/down array of equivalent fibrils $\beta_n = \pm\beta_{\text{fibril}}$, where the sign is chosen randomly for a given circle, and β_{fibril} is assumed constant for all circles. The numerically calculated scattering curve is shown in Fig. 7. Two points may be noted. (*a*) This calculated curve is a remarkably good simulation of the measured data of Fig. 4, and agrees well with the analytical results of Eq. 8. (*b*) There is no sharp peak at zero angle, thereby verifying

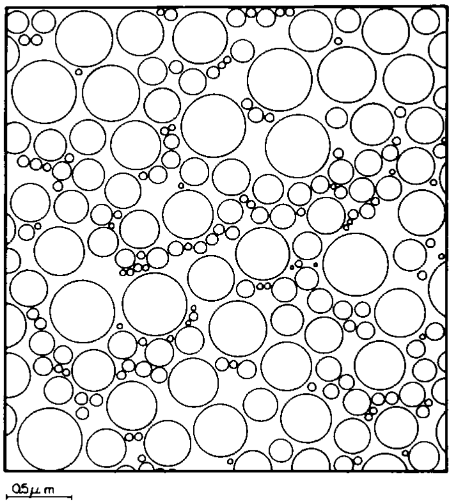

FIGURE 6 Typical region of computer model of the collagen fibrils in rat-tail tendon. The model corresponds to a transverse section and is used to explore numerically the SH generating properties of this tissue and to provide a basis for comparison with both analytical approximations and experimental data. The fibril diameter distribution and density matches the parameters known for 3-mo-old animals. The figure bears a remarkable resemblance to electron micrographs of transverse sections of real tendons.

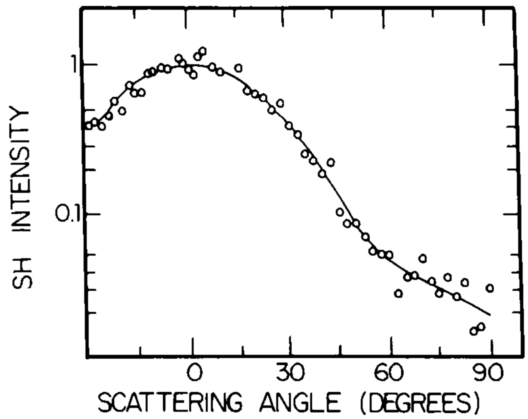

FIGURE 7 SH scattering from the model of Fig. 6 in which the signs of the fibrils are chosen randomly +/−. The circles (O) are numerically calculated data using Eqs. 9 and 4 for an array of 250,000 fibrils arranged as a sample of thickness $T = 25$ µm and width $W = 0.6$ mm. Since the random +/− array may be considered as a pure noise signal and the scattering curve as its power spectrum, one would expect that the scattering curve for an infinitely large sample be perfectly smooth. This is correct but the smooth infinite limit is approached in an unexpected way. The scattering curve of a finite sample consists of a very large number of rapid oscillations whose minima are essentially zero and whose maxima are on the average twice the expected scattering intensity. The average spacing of these oscillations is λ_2/n_2W, which in our case is ~0.6 mrad. In the limit $W \rightarrow \infty$ these oscillations crowd together, ultimately approaching the expected smooth limit. In our experiments the equivalent scattering curves are measured with a finite angular resolution much greater than 0.6 mrad, so the oscillations are effectively damped out. Accordingly, the data of the numerical simulation displayed here are averaged over a ±1° interval and this average is what is plotted in the figure. The result may be seen to bear a remarkable resemblance to the measured data of Fig. 4. (The greater relative smoothness of the measured data may be due either to presently not fully understood additional smearing effects, or to a +/− distribution that is truly smoother than that generated by purely random statistics—this latter possibility, if correct, would be biologically significant.) The solid curve shown here is the same as in Fig. 4, and is calculated from Eq. 8 using the same parameters. This simulation demonstrates that the analytical approximations leading to Eq. 8 are fully applicable to rat-tail tendon and that SHG by the collagen fibrils is well understood. It also shows that the random clusters shown in Fig. 5 do not lead to an intense, sharp peak at the origin.

directly that random local deviations from equal numbers of up/down fibrils do not produce such a peak. Accordingly, the origin of this peak must be sought elsewhere.

Could up fibrils, for example, have a larger value for β than do down fibrils, so that a random up/down array would still show a net polarity? Our measurements appear to eliminate this possibility. The data in Fig. 4 were measured with a slit width of 1.5°, while the intrinsic angular divergence produced by an ordered sample 0.5 mm in width is 0.7 mrad. The coherent peak height in Fig. 4 must thus be corrected appropriately. To produce a calculated coherent peak of the corrected magnitude, our computer model tells us that up fibrils would need to have a β which is two times larger than that of down fibrils. Since the fibrils are composed almost exclusively of parallel collagen molecules, the fibril β simply reflects the β of collagen itself. A twofold difference in β between up and down fibrils implies either that the structure of collagen is markedly different in the two fibril types, or that the collagen density differs by a factor of 2. The banding patterns seen under the electron microscope (18) eliminate both possibilities: no difference in quarter-stagger or other details of the complex banding patterns that are directly tied to the detailed molecular structure (30) are seen for up vs. down fibrils, while the density of the staining does not vary systematically from one fibril type to the other, as would be required for a twofold variation in collagen density.

Having thus concluded that the random up/down array of polar collagen fibrils, cannot be the source of tendon polarity, we turn to a detailed description of our work on the newly discovered polar structures.

SECOND HARMONIC MICROSCOPY

Instrumentation and Operation

The scanning SH microscope was first proposed by Sheppard and Kompfner and developed by them and their co-workers to the point where good-quality SH images of crystal plates were obtained (14–17). The use of SH microscopy for the study of biological tissue was also proposed but not implemented, presumably because of lack of adequate sensitivity: the SH signals from RTT, for example, are some three to five orders of magnitude smaller than from crystal plates.

In Fig. 8 we show a schematic of our SH microscope. A 1.064 µm, 5 pps, multimode, Q-switched Nd-YAG laser is used for excitation. Condenser II produces the small scanning spot, slit S_1 controls the convergence of the laser beam in the XY plane, while slit S_2 selects one of two distinct imaging modes. If the object exhibits polar

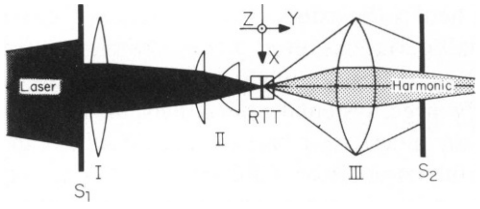

FIGURE 8 SH microscope. Slit S_1 controls the convergence of the incident laser beam, while slit S_2 selects either the coherent or incoherent imaging mode; in the figure it is set for coherent imaging. The long tendon axis (the Z axis) is normal to the plane of the figure, and the sample is scanned raster-fashion under the stationary laser spot. When a low resolution SH scattering curve of a particular sample feature is required, slit S_2 is scanned appropriately. When high-resolution scattering data are needed, condenser II and objective III are slid out of the beam path, and slit S_2 is narrowed and scanned. With the condenser in place the spot size is effectively ~50 µm, and the width of S_2 is normally set to correspond to an angular resolution of 2°. Without the condenser the spot size is ~0.5 mm and S_2 is normally narrowed so that the effective instrumental resolution is ~2 mrad. Additional features of the microscope are discussed in the text.

ordering over dimensions large compared to λ_l then a coherent, forward-directed SH beam is generated whose angular divergence is determined either by the size of the object itself, or by the convergence and spot size of the laser beam. The polar filaments and patches are of this nature. The collagen fibrils, on the other hand, are all smaller than λ_l and the random up/down array produces the broadly divergent incoherent SH scattering of Fig. 4, as discussed previously. These two types of structures give rise to two different modes of imaging for the SH microscope, coherent and incoherent. In the coherent mode only a narrow, forward-directed beam is accepted by slit S_2 which is located on the optical centerline: this picks out the sharp, coherent central peak of Fig. 4. In the incoherent imaging mode slit S_2 is moved a few degrees off center, and so passes only part of the broad, incoherent scattering associated with the collagen fibrils.

In the coherent mode S_2 also passes part of the incoherent background, so that the extent of coherent/incoherent discrimination is determined in part by the width of the slit and the convergence of the laser beam, and in part by the intrinsic nature of the sample. There is no practical advantage in making S_2 smaller than the coherent SH beam size, which is determined by the convergence of the laser. Accordingly, this convergence, and hence for a given focal-length condenser the width of S_1, is the major instrumental parameter controlling the coherent/incoherent contrast ratio. If the laser beam convergence is $\Delta\theta$, then the classical microscope resolution formula (31) predicts a spot size $d \approx \lambda_l/\Delta\theta$, so that the instrumental resolution and coherent/incoherent contrast are coupled, and must be optimized for each sample. In the case of RTT a suitable value is $\Delta\theta = 2°$, which yields an adequate contrast ratio and a calculated value for $d \approx 30\ \mu\text{m}$. In practice d was found to be rather larger due principally to two factors: (*a*) aberrations in the simple spherical lenses used to construct the condenser (cemented microscope objectives "burned" in the intense laser beam), and (*b*) astigmatism of the laser beam itself, which forced a compromise between horizontal and vertical focusing. This astigmatism arose from nonuniform pumping of the Nd-YAG rod and the thermal lens effect (32). SHG depends upon the square of the laser intensity, so the effective SH spot size is smaller than the linear optical value and in our instrument was approximately 50 μm.

In addition to the optical train shown in Fig. 8, our SH microscope contained (*a*) a reference arm in which SHG in crystalline quartz was used to normalize out laser power fluctuations, (*b*) a half-wave plate for rotating the laser polarization, and (*c*) a detection system consisting of an analyzing polarizer, narrow-band interference and blocking filter, and a high quantum efficiency photomultiplier. The sample and reference arm signals were processed by fast electronics that included gain-controlled amplifiers, fast analog gates, pulse stretchers, and analog-to-digital converters. Scanning was accomplished by moving the sample raster-fashion under the stationary laser spot. The microscope was controlled by an Apple II+ computer (Apple Computer Inc., Cupertino, CA) which also stored, processed, and displayed the data. Typically, SH images containing five-to-seven thousand 50 μm^2 pixels were obtained, with each pixel representing an average of 10 laser shots, so that collection of data for a complete image required about 5 h. With straightforward improvements in instrumentation a two-order-of-magnitude reduction in scan time should be possible, while with a suitable laser oscillator-amplifier combination and sensitive CCD camera, detection of a complete image could be obtained in a single (nano- or picosecond) laser pulse. Although not employed here, a form of SH interference microscopy should also be possible in which the sample signal is mixed with the SH from a reference material such as quartz; this would provide an additional level of contrast based upon variations in the phase of $\beta(\mathbf{r})$.

SH Images—Filaments

In Fig. 9 *a* we present a coherent SH microscope image of a tail tendon from a 3-mo-old animal, and in Fig. 9 *b* an incoherent image of the same sample. The differences between the images are striking: Fig. 9 *b* shows the relatively uniform distribution of the collagen fibrils, while Fig. 9 *a* reveals a highly filamented network of polar structures.

The data in Figs. 9 *a–b* were taken with a step size equal to the scanning spot size *d*. This was necessitated by experimental limitations reinforced by our currently limited graphics capability, and results in a significant loss of fine detail. Accordingly, Fig. 9 *a* displays only the gross distribution of the filamentous network that permeates the tendon. In Fig. 9 *c* we display a line scan of the bottom edge

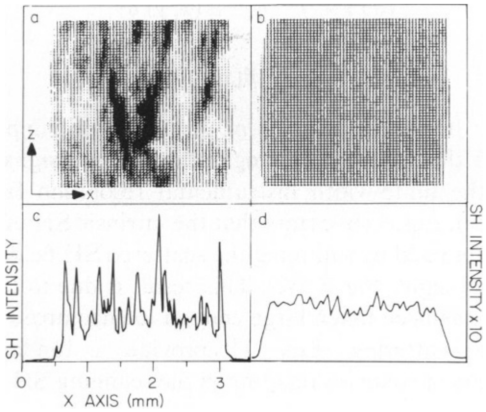

FIGURE 9 (*a*) Coherent, and (*b*) incoherent SH microscope images of a 3-mo-old tendon. The images are negative, i.e., dark regions are areas of strong SHG. The pixel size is 50 μm^2 and the image in (*a*) is overexposed so as to bring out weaker features. (*c*) High resolution coherent line scan of the bottom edge of (*a*) showing the large number of fine polar filaments that permeate the tendon. (*d*) Incoherent line scan of bottom edge of (*b*) showing minor variations in the fibril matrix. The absolute intensity scale in (*d*) is one-tenth that of (*c*). The *X* axis scale is the same for *a–d*.

of Fig. 9 *a* in which the step size is one-fifth the spot size: visible here are some 25–30 filaments. Since it is difficult, if not impossible, to convey quantitative intensity information via a grey-scale, we replot the data of Fig. 9 *a* as an isometric view in Fig. 10, where the heights of the features are proportional to their SH intensity. Close study of this figure in conjunction with Fig. 9 *a* suggests the presence of numerous transverse connections between the filaments, leading to the possibility that these form an interconnected network.

Imaging Theory and Imaging Artifacts

All forms of microscopy are capable of producing imaging artifacts, the nature of which depends upon the means of contrast production. This is also true of coherent SH microscopy, especially in samples whose thickness is of order, or greater than, the SH coherence length ℓ_c. If we locate the center of the scanning spot at $x = x_o$, and assume that the detection system accepts a range of angles $\Delta\Omega$ about the forward direction, then the measured SH microscope signal may be written

$$S_2(x_o) = \int_{\Delta\Omega} \mathrm{d}\kappa_x \left| \int_{-\infty}^{\infty} \mathrm{d}y \int_{-\infty}^{\infty} \mathrm{d}x\, e^{i(\kappa_x x + \kappa_y y)} \cdot [E^{(1)}(x_o - x)]^2 \beta(x, y) \right|^2. \quad (10)$$

Here we have assumed that the depth-of-focus (Rayleigh range) of the focused laser beam is much greater than the sample thickness. If we further assume that $E^{(1)}(\mathbf{r})$ is of uniform phase along x (quasi-plane-wave) and write $[E^{(1)}(x_o - x)]^2 = I_1(x_o - x)$, where $I_1(x)$ is the laser intensity profile, we have, after extending $\Delta\Omega$ so as to include all of the coherent scattering,

$$S_2(x_o) = \int_{-\infty}^{\infty} \mathrm{d}x I_1^2(x_o - x) I_2(x), \quad (11a)$$

$$I_2(x) = \int_{-\infty}^{\infty} e^{-i\kappa_y y} \mathscr{a}(x, y)\, \mathrm{d}y, \quad (11b)$$

$$\mathscr{a}(x, y) = \int_{-\infty}^{\infty} \mathrm{d}v\, \beta(x, v) \beta(x, v + y). \quad (11c)$$

Eq. 11a, in which a factor of 2π has been suppressed, expresses the usual broadening of the intrinsic signal $I_2(x)$ due to the finite-width instrumental resolution function $I_1^2(x_o - x)$. Eqs. 11b–c state that the intrinsic SH intensity $I_2(x)$ is obtained by summing the scattered SH fields along the line-of-sight, the Y axis. This result is due to the fact that $\Delta\Omega$ has been taken large enough to encompass all the coherent scattering. Eqs. 11 provide a fundamental description of coherent imaging in the scanning SH microscope.

As a simple, practical example of possible artifacts we consider two very thin, overlapping filaments separated by distance ℓ, as in Fig. 11 *a*. We take these filaments to have a Gaussian profile along the X axis and write

$$\beta(x, y) = \beta[e_1(x)\delta(y) + e_2(x)\delta(y - \ell)], \quad (12a)$$

$$e_i(x) = \exp(-x^2/w_i^2). \quad (12b)$$

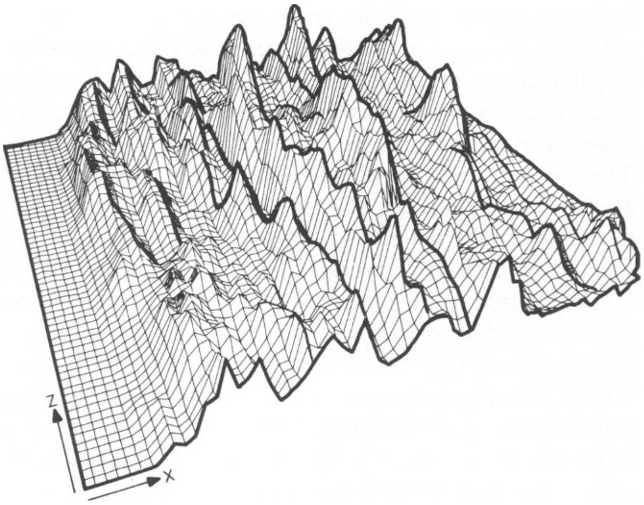

FIGURE 10 Isometric view of the coherent SH microscope data of Fig. 9 *a*. The heights of the features are proportional to the SH intensity.

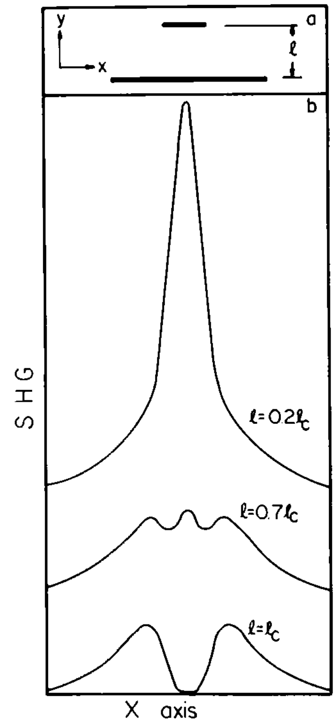

FIGURE 11 Coherent SHG by two overlapping filaments spaced by distance ℓ along the line-of-sight. (*a*) The model used in which the widths of the bars are the widths of the Gaussians chosen to represent each filament. (*b*) Coherent SH intensity, Eq. 13, for various spacings; here ℓ_c is the SH coherence length, Eq. 6. Note that depending upon ℓ/ℓ_c an X axis scan could lead to the conclusion that the object contains either one, two, or three filaments. These results illustrate the need for additional information about what is happening along the line-of-sight in order to properly interpret coherent SH data.

Assuming further that the scanning spot size $d \ll w_1, w_2$, so that we may write $I_1^2(x_o - x) = \delta(x_o - x)$, we immediately obtain

$$S_2(x_o) = \beta^2[e_1^2(x_o) + e_2^2(x_o) + 2e_1(x_o)e_2(x_o)\cos(\pi\ell/\ell_c)]. \quad (13)$$

Eq. 13 is plotted in Fig. 11 *b* for different values of ℓ/ℓ_c. As is evident, a variety of erroneous conclusions can be drawn from a coherent SH microscope image when overlapping structures are present. This, of course, is always true in all coherent imaging methods, such as, for example, phase-contrast microscopy. When quantitative results are required, some independent means must be had for determining what is happening along the line-of-sight. In the present work this will be supplied by crossed-beam SHG.

SH Images—Patches

In Figs. 12 *a–g* we present coherent SH microscope images for tail tendons from 1, 3, and 6-mo-old animals. There do not appear to be any obvious, systematic age differences. One striking feature of these images is the strong irregular patch-like areas. In Figs. 12, *c, f,* and *g* these patches extend out to the image edges, while in Figs. 12, *a* and *b* they are close to the edge. Since the image edges also correspond to the tendon surface, where the polar patches touch the edge they must also contact the tendon surface. The simplest hypothesis is that the patch as a whole lies on or near the surface, as in Fig. 12 *h*, and we believe this to be the case. The evidence here is the observation that from the point of view of SHG the central patches in Fig. 12 *e* are "thin," i.e., their thickness along the line-of-sight is much less than ℓ_c; this conclusion follows from crossed-beam SHG studies discussed in the next section. The counter hypothesis to the surface patch is a near radial slab, as indicated in Fig. 12 *i*. But, as is also indicated there, such a slab would be expected to crumple when compressed radially and would thus appear to be "thick," in conflict with observation. Although an absolutely unambiguous determination of the positions of the patches will undoubtedly await their visualization by electron microscopy, we believe the evidence currently available is sufficient to support a surface location as a working hypothesis. What about the filaments? Are these also located on the tendon surface? In a later section we will describe small-angle SH scattering experiments that show that the filaments permeate the tendon cross-section in an apparently random fashion.

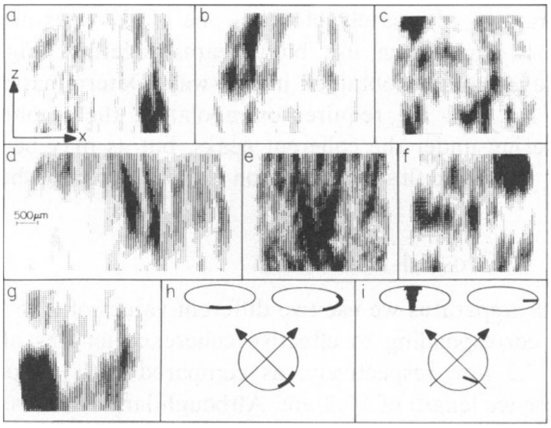

FIGURE 12 Coherent SH microscope images of tail tendons each from a different rat. Animal ages are (*a–c*) 1 mo, (*d–f*) 3 mo, and (*g*) 6 mo. Image processing parameters are the same as for Fig. 9 *a*, while the scale for all images is shown in *d*. In all images the proximal end of the tendon is uppermost except for *e*, where documentation of the tendon ends was inadequate and the orientation is uncertain. (*h*) Compression along one of two different directions of a tendon containing a surface patch. Depending upon direction the result is a thin area located either at the sample center or the sample edge. (*i*) Compression of a near-radial slab resulting in a thick region at the sample center or a thin region at the sample edge. Since the central patches in *e* are known to be thin, the model for this, and the other tendons, is assumed to be *h*.

CROSSED-BEAM FREQUENCY SUMMATION

As has become apparent, the thickness of the filaments and patches is an important parameter required for quantitative interpretation of our SH microscope images, an estimate of the volume fraction of the polar structures and hence their degree of polarity, and also, as described in the next section, thickness data is required for analysis of small-angle SH scattering measurements that yield the relative signs and Y axis distribution of the filaments. Accordingly, we developed the crossed-beam technique described below, and used it to estimate the thickness of a large number of filaments and patches.

Theory

SHG from an ordered, plane-parallel slab illuminated by crossed laser beams making angles $\pm\theta$ with respect to the slab normal, the Y axis, as in Fig. 13, may be written as a sum of three terms,

$$I_2 = I^{+\theta}(+\theta) + I^{-\theta}(-\theta) + I^{\pm\theta}(0). \quad (14)$$

Here the notation $I^{\alpha}(\beta)$ implies that a laser beam propagating with angle α relative to the Y axis generates a SH beam that propagates with angle β. The first two terms on the R.H.S. of Eq. 14 represent SHG from each incident laser beam separately; the last term corresponds to frequency summation of the two ($\pm\theta$) laser beams, which gives rise to an SH beam at zero angle. This behavior follows from Eqs. 1 and 4 by writing the field at the incident frequency ω_1 as the sum of the fields from the two incident laser beams. For the $I^{\pm\theta}$ term in Eq. 14, κ in Eq. 4c is replaced by

$$\kappa(\theta) = \mathbf{k}_2 - (\mathbf{k}_1^{+\theta} + \mathbf{k}_1^{-\theta}); \quad (15)$$

and

$$\kappa(\theta) = k_2 - 2k_1\cos\theta. \quad (16)$$

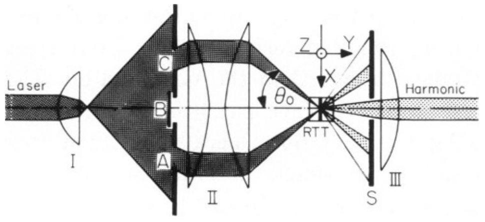

FIGURE 13 Crossed-beam SH microscope. The various apertures, of which only three, *A–C*, are shown, could be either uncovered or blocked so as to create different beam configurations. A configuration is labeled by the values of θ_0 for the beams used. A single beam with $\theta_0 = 0°$ would be labelled as a 0° configuration, while the configuration shown in the figure with θ_0 equal +10° and −10° for the two beams respectively would be labeled as ±10°. Slit S could be positioned at any of the coherent SH beams so as to yield different coherent images, or it could be located between the coherent beams so as to yield an incoherent image. The appropriate images were obtained by fixing the slit and scanning the sample raster-fashion under the crossed-beam spot. For coherent imaging S was usually located at zero angle (the optical centerline), as shown. This slit could also be scanned to provide low-resolution SH scattering data. The use of this microscope to obtain thickness data and information on what is happening along the line-of-site, the *Y* axis, is described in the text.

In Fig. 14 we display a typical data set obtained with the crossed-beam SH microscope of Fig. 13. The thickness *t* of our plane-parallel model slab (filament or patch) is extracted from such data as follows. Distinguishing once again between coherent (coh) and incoherent (inc) SHG, and defining

$$\rho_{\mathrm{coh}} \equiv I^{\pm\theta}_{\mathrm{coh}}(0) / \sqrt{I^{+\theta}_{\mathrm{coh}}(+\theta) I^{-\theta}_{\mathrm{coh}}(-\theta)}, \tag{17}$$

we may write

$$\rho_{\mathrm{coh}} \simeq \frac{\ell_c^2(\theta) \sin^2[\pi t/2\ell_c(\theta)]}{\ell_c^2 \sin^2[\pi t/2\ell_c]} \cdot \frac{4\langle |\mathrm{E}_{+\theta}|^2 |E_{-\theta}|^2\rangle}{\sqrt{\langle |E_{+\theta}|^4\rangle \langle |E_{-\theta}|^4\rangle}}, \tag{18}$$

where

$$\ell_c(\theta) \equiv \pi/\kappa(\theta) \simeq \frac{\lambda_1}{4n_1}\left[\frac{n_2 - n_1}{n_1} + \frac{1}{2}\left(\frac{\theta_o}{n_1}\right)^2\right]^{-1}, \tag{19}$$

unimportant factors of $\cos\theta \simeq 1$ have been suppressed, and ℓ_c is, to sufficient accuracy, as given in Eq. 6. On the R.H.S. of Eq. 19, θ_0 is the (relatively small) external angle of incidence before correction for refraction. In effect, varying θ permits us to vary ℓ_c, and since SHG depends upon t/ℓ_c, t may be determined.

$I^{\pm\theta}$ depends upon the amplitudes and extent of overlap of the electric fields, $E_{+\theta}$, $E_{-\theta}$, of the two laser beams and the last factor in Eq. 18 accounts for this in terms of a spatial average over the beam overlap profile. (Assumed here is that deviations from the average are random). A determination of t from a measurement of ρ_{coh} requires, therefore, a knowledge of this beam overlap factor. Note that if $t \ll \ell_c$ and $\ell_c(\theta)$, then ρ is equal to this factor, and so SHG from sufficiently thin objects can be used to calibrate the apparatus. The natural candidate here is the random up/down array of collagen fibrils that surrounds the filaments and patches, and thus provides a ready-made, built-in standard. One possible complication is the fact that the scattering pattern of the individual fibrils is much broader than $\pm\theta$, so that there exists the possibility of coherent, inter-beam interference effects between the three SH beams. In practice this interference is not realized, in part due to the multi-mode nature of the laser, which limits the transverse coherence of the beam incident on the apertures of Fig. 13 to something less than the aperture spacing. In addition, one would expect that any such interference effects would vary during the course of the laser pulse, and from pulse to pulse, and so would average out to zero. Experimentally, we find that deliberately varying the phase (optical path) of one of the beams has no detectable effect. We therefore assume

$$\langle E^{k}_{\alpha} E^{\ell *}_{\beta} E^{m}_{\gamma} E^{n *}_{\delta} \rangle \simeq \langle |E^{k}_{\alpha}|^2 |E^{m}_{\beta}|^2 \rangle \, [\delta_{\alpha\beta}\delta_{\gamma\delta}\delta_{k\ell}\delta_{mn} + \delta_{\alpha\delta}\delta_{\beta\gamma}\delta_{kn}\delta_{\ell m}], \tag{20}$$

where the notation E^{k}_{α} implies the *k*th power of the electric field of a laser beam propagating at angle α relative to the *Y* axis. Eq. 20 states that in calculating SHG by the fibrils in the presence of two laser beams all terms depending upon the relative phases of the two beams vanish in the expression for the intensity. We thus have for the incoherent SH scattering of the fibrils,

$$\rho_{\mathrm{inc}} \equiv \frac{I^{\pm\theta}_{\mathrm{inc}}(0) - I^{+\theta}_{\mathrm{inc}}(0) - I^{-\theta}_{\mathrm{inc}}(0)}{\sqrt{I^{+\theta}_{\mathrm{inc}}(+\theta) I^{-\theta}_{\mathrm{inc}}(-\theta)}} \simeq \frac{4\langle |E_{+\theta}|^2 |E_{-\theta}|^2\rangle}{\sqrt{\langle |E_{+\theta}|^4\rangle \langle |E_{-\theta}|^4\rangle}}. \tag{21}$$

To obtain ρ_{inc} we first measure SHG by each beam separately—alternately blocking one of the apertures of Fig. 13—and then use both beams together: Fig. 14 displays the data obtained in this way. Determination of $I^{+\theta}_{\mathrm{inc}}$, $I^{-\theta}_{\mathrm{inc}}$ and $I^{\pm\theta}_{\mathrm{inc}}$ requires extrapolating the incoherent scattering under the coherent peaks, but as may be seen from the figure this extrapolation is easily accomplished.

Crossed-Beam Data

In our apparatus we use two different values of θ_0, 5° and 10°, corresponding to effective coherence lengths of 9.3 and 7.2 μm, respectively, as compared with a normal coherence length of 10.2 μm. Although larger values of θ_0 could have proven useful, the effects of spherical and other lens aberrations proscribed these, while an apparatus containing beam splitters, separated mirrors, etc., was found to be insufficiently stable for long term use as compared to the monolithic arrangement of Fig. 13. An ideal (maximal) value for ρ_{inc}, arising when $E_{+\theta}$ and $E_{-\theta}$ are everywhere in phase, is $\rho_{\mathrm{inc}} = 4$. For uniform, perfectly overlapped laser beams of random relative phase we could expect $\rho_{\mathrm{inc}} = 2$. Experimentally, we were able to achieve values that were close to but somewhat less than this, when special pains were taken to ensure that the sample lay in the plane of

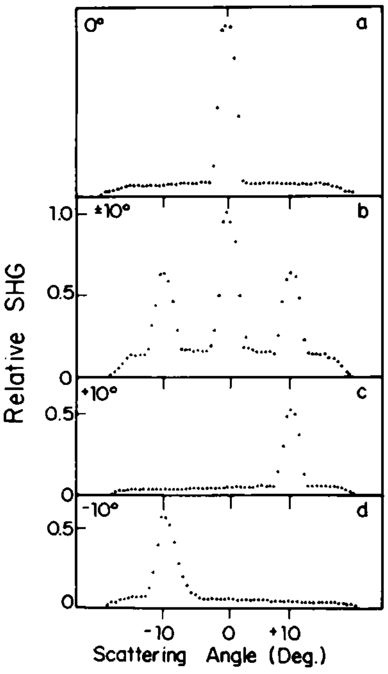

FIGURE 14 Crossed-beam SH scattering data for a surface patch obtained by scanning slit S of Fig. 13. The labeling of the beam configurations is explained in the caption of Fig. 13. The configurations used here are (*a*) 0°, (*b*) ±10°, (*c*) +10°, and (*d*) −10°. The sharp peaks correspond to coherent SHG by the patch, and the diffuse background corresponds to incoherent SHG by the surrounding fibril matrix. The use of such data in conjunction with Fig. 15 *a* to measure the thickness of the patch is described in the text.

maximal beam overlap and the laser had been operated sufficiently so as to reach thermal equilibrium.

From Eqs. 18 and 21 it follows that the relevant parameter for determining t is ρ_{coh}/ρ_{inc}, which is plotted in Fig. 15 *a*. We measured this ratio for $\theta_0 = 10°$ for 17 different isolated filaments in tail tendons from three different animals and in about 80% (14) of the cases found values between 0.8–1.1. From Fig. 15 *a* we can conclude that the filament thicknesses were, within error, either between 0–5 μm, or between 17.4–17.8 μm, this latter possibility being suspect because of its highly fortuitous nature. Experimentally, the $\theta_0 = 5°$ data also yields values of ρ_{coh}/ρ_{inc} close to unity, so we conclude that most of the filaments are thin, with 2–3 μm being an approximate average thickness. The major deviations from "thinness" usually occurred for areas of very weak coherent SHG in which the coh/inc intensity ratio was not much greater than unity. In Fig. 16 we show two examples in which ρ_{coh}/ρ_{inc} is either much less than, or much greater than unity, corresponding to "thick" areas in the range 12–20 μm. We believe these data are best interpreted in terms of a fine, unresolved, dilute network of coherent SH generating material that permeates the whole tendon volume, leading to regions which are thick but nonetheless weak SH generators. We note in this respect that virtually every area of every tendon shown in Fig. 12 showed some coherent SHG (in addition to the usual zero-angle incoherent SHG) even when no specific structures were visible.

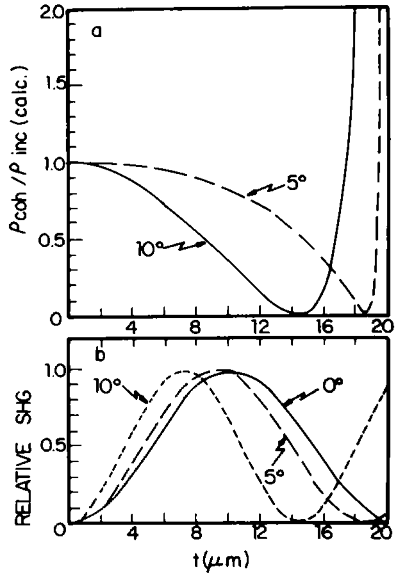

FIGURE 15 (*a*) Calculated ratio of Eq. 18 to Eq. 21 vs. object thickness *t* for crossed-beam configurations ±5° (---) and ±10° (——). This graph can be used with measured data, as in Fig. 14, to determine absolute thicknesses. (*b*) Calculated intensity of SHG with slit S of Fig. 13 located on the optical centerline (zero angle) vs. object thickness *t* for a single 0° beam (——) and crossed-beam configurations ±5° (---) and ±10° (···). The use of this graph together with appropriate data to determine relative thicknesses of different objects is described in the text.

Relative Thickness

Once the thickness of a given filament or patch has been measured by the above (somewhat laborious) method, it can, in principle, serve as a standard, and the thicknesses of adjacent structures may be estimated by simply comparing

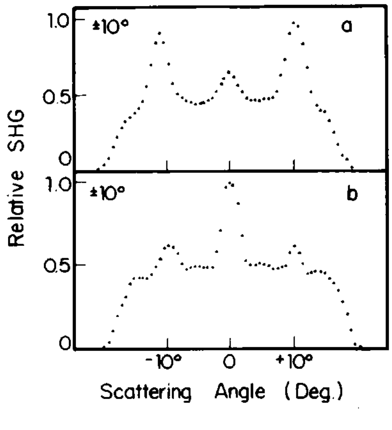

FIGURE 16 Crossed-beam scattering data (±10° beam configuration) for two different tendon areas that show weak coherent SHG. These data are appropriate to thick areas that are weakly polar. Based upon Fig. 15 *a* the thickness of *a* may be estimated to be in the region of 12–16 μm, while that of *b* is of order 18–20 μm. Such data are typical of areas between filaments or patches in which no special structures are visible but which nonetheless still show some coherent SHG.

relative intensities for normal incidence, $\theta = 0°$, and crossed beams, $\theta = \pm 5°$, $\pm 10°$: reference to Fig. 15 *b* will clarify this. For example, a 3-μm- and a 17.5-μm-thick patch will both have very nearly the same SH intensity for $\theta = 0°$ and also for $\theta = \pm 10°$, but for $\theta = \pm 5°$, $I(3\ \mu\text{m})/I(17.5\ \mu\text{m}) \simeq 5$. In fact we find that either the structures are all thin and so their relative intensities change little from one beam configuration to another, or else, when changes do occur, they are not describable as being due either to thick or to overlapping structures, as the following examples illustrate.

Crossed-Beam Images

In Fig. 17 *a–c* we compare coherent SH microscope images obtained for $\theta = 0°$, $\theta = \pm 5°$, and $\theta = \pm 10°$; while in Fig. 17 *d* we present a labeled schematic of the various structures observed. The center of patch P_1 was directly measured to be ~3 μm in thickness, and this, then, can serve as an internal thickness standard. The region labeled *A* in Fig. 17 *d* shows a marked reduction in relative intensity for the $\theta = \pm 10°$ image, as compared to the $\theta = 0°$ and $\theta = \pm 5°$ images. If we divide the coherent SH intensity at *A* by that at P_1 for each of the three images we obtain 0.88, 0.91, and 0.42 for $\theta = 0°$, $\pm 5°$, and $\pm 10°$ respectively, and since we are simply dealing with relative intensities within the same image, measured values should be rather accurate. The value 0.42 for $\theta = \pm 10°$ implies (via Fig. 15 *b*) that region *A* has a thickness of either 12.6 or 16.3 μm. The former value is immediately eliminated since it would require that at $\theta = 0°$, A be 4.4 times as intense as P_1, in marked contrast to the measured value of 0.88. The 16.3-μm thickness, is also in conflict with observation but to a lesser extent, since now *A* need be only 1.9 times P_1, but this is still much greater than any possible experimental error. Similar conflicts occur for the other circled regions in Fig. 17, leading to the conclusion that the differences in relative intensity that show up in the $\theta = \pm 10°$ image as compared to the $\theta = 0°$ image cannot be simply attributed to thickness variations. Since these regions appear to be areas in which different filaments or patches overlap, we have also sought to interpret the observed differences on this basis, but again with no definitive success.

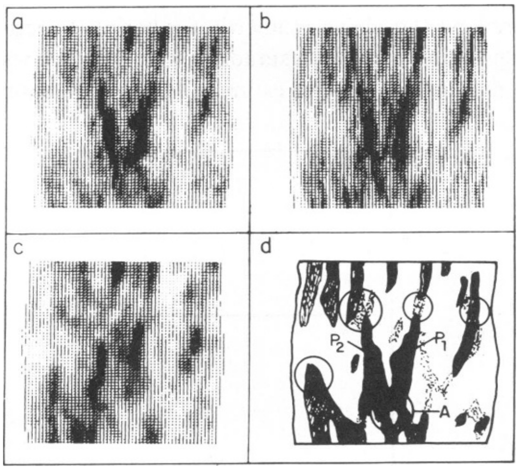

Figure 17 Crossed-beam coherent SH images for beam configurations (*a*) 0°, (*b*) ±5°, and (*c*) ±10°. The data were obtained with slit S of the crossed-beam microscope located at zero angle as shown in Fig. 13. (*d*) A schematic representation of the image of *a* in which the central patches are labeled P_1 and P_2, and the region in which they appear to overlap is labeled *A*. Both A and the other circled regions show significantly different relative intensities between the 0° image of *a* and the ±10° image of *c*. The other circled regions appear to also be areas of overlap between different structures. An extensive discussion of these overlap regions is given in the text.

Overlaps

Take region *A* once more as an example. This appears to be a region of overlap between P_1 and P_2, which, since these have approximately the same intensity $[I(P_2)/I(P_1) = 0.8]$ can be concluded to have about the same thickness $[t(P_2)/t(P_1) = 0.9]$. Then, the simple model of Fig. 18 is applicable, but as may be seen from this figure, no value of *t* yields a reasonable match between measured and calculated intensity ratios. A similar situation holds for the other circled regions in Fig. 17.

We suspect that something like the following is happening. Region *A*, and the other circled regions, may correspond to areas in which patches or filaments located at

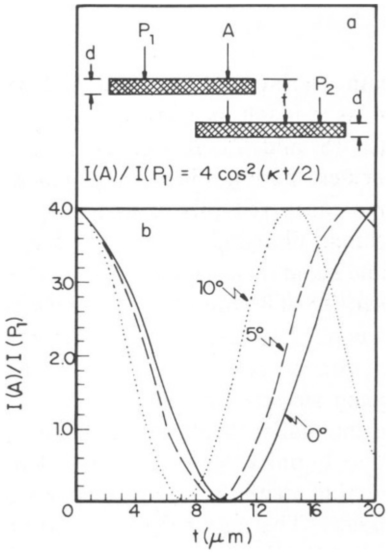

Figure 18 (*a*) Simplest possible model of overlap region of patches P_1 and P_2 of Fig. 17 *d*. The ratio of the coherent zero-angle SH intensity at *A* and at, say, P_1, $I(A)/I(P_1)$, is independent of the patch thickness *d* but depends upon the patch's separation *t* and the momentum transfer κ. κ, in turn, depends upon the beam configuration used, as given in Eq. 16. The factor of 4 in the equation shown is due to the fact that the total amount of polar material at *A* is twice that at P_1. (*b*) $I(A)/I(P_1)$ vs. the patch's separation *t* for beam configurations 0° (——), ±5° (---), and ±10° (···). As discussed in the text the measured data do not at all fit the model shown, but suggest instead a more complicated model in which the patches merge continuously in such a way that the total amount of polar material in the overlap region *A* is the same as in the isolated patches.

different depth levels interconnect. These interconnections are, because of the level differences, "thick," and so the ±10° images show much reduced relative intensities. The total amount of polar material in these interconnections is, however, about the same as elsewhere, so that such regions, although thick, are not anomalously strong SH generators. Accordingly the factor of four in the model of Fig. 18, which arises from the twofold increase in SH-generating material in the overlap region, should be suppressed. When this is done a reasonable level of agreement is obtained with experiment. Since we have not found an independent means for confirming the above hypothesis, all we can definitely state is that although the filaments and patches are generally thin, there are also some number of diffusely thick areas located in regions of apparent overlap.

Degree of Polarity

If we assume an average 2–3-μm thickness for the polar structures and estimate the fractional area these cover in our SH microscope images, we conclude that the volume fraction of polar material is a few percent. Since the volume average piezo- and pyroelectric coefficients (1, 6) are also of this order relative to strongly polar systems, we can deduce that the polar structures are strongly polar, and thus that this polarity may well be biologically functional.

Computer Simulation

Are the filaments simply regions containing some net excess of up fibrils? Our computer simulation shows that the coherent/incoherent SH intensity ratio observed for the filaments and the surrounding fibril matrix requires all fibrils comprising a filament to point up, while in many cases even this is insufficient, thereby calling into question the possibility that the polar filaments and patches are composed of collagen fibrils.

SMALL-ANGLE SH SCATTERING

We turn now to a determination of the relative signs (directionality) of the polar filaments and their distribution along the Y axis. Although we have argued that the polar patches are surface features, no evidence for either a surface or bulk location for the filaments has yet been provided. Here we discuss our small-angle SH scattering measurements, which show that most, if not all, polar filaments are of the same sign, and that these filaments permeate the tendon bulk in an apparently random fashion.

Theory—Relative Signs

Consider a pair of similar filaments separated by some distance Δx along the X axis, but with zero separation along the Y axis ($\Delta y = 0$). If both filaments have the same directionality, then for SHG in the forward direction (zero scattering angle) constructive interference occurs and a sharp zero-angle peak is produced. In addition to this there will also be a number of weaker side lobes whose locations and intensities depend upon both Δx and the filaments' widths. If the filaments have opposite directionality then for forward SHG the interference is destructive and the scattering pattern will show a pronounced dip at zero angle. Since the scattering patterns are so characteristic, a sharp peak or a pronounced dip, the relative signs of the filaments may be simply read off by inspection.

Sign Ambiguity

If $\Delta y \neq 0$, however, a significant complication occurs which we describe in somewhat more general terms. We start by reformulating Eq. 4. Suppose we have N filaments which are well separated so that it makes sense to talk about SH scattering by N discrete objects. Then, just as is the case in x-ray diffraction, the structure factor of Eq. 4 is conveniently written in terms of form and phase factors as

$$G(\kappa_x, \kappa_y) = \sum_{n=1}^{N} \hat{\beta}_n(\kappa_x, \kappa_y) e^{i[\kappa_x x_n + \kappa_y y_n]} \tag{22}$$

Here $\hat{\beta}_n(\kappa)$ is the nth filament form factor (i.e., the Fourier transform of $\beta(\mathbf{r})$ for that filament), the coordinates (x_n, y_n) locate the filament center, and we assume for simplicity filaments that are symmetric in x and y. In keeping with the results of the previous section we further assume that the filaments are so thin that we can write

$$\hat{\beta}_n(\kappa_x, \kappa_y) = \beta_n f_n(\kappa_x), \tag{23}$$

where $f_n(\kappa_x)$ is the usual form factor for the given filament, and the sign of β_n depends upon the filament directionality, being + for, say, up-pointing filaments and – for those that point down. In our compressed samples the filaments are necessarily smeared out along the X axis, as in Fig. 3 *b*, so that the $f_n(\kappa_x)$ fall off rapidly with scattering angle and thus restrict the measurable SH scattering to the small-angle regime ($\theta \lesssim 1$–$2°$). In this regime κ_y (Eq. 5b) is essentially independent of θ and is equal to π/ℓ_c.

We now come to the ambiguity: with the above assumptions and restrictions, which are fully appropriate to our samples, we can rewrite Eq. 22 as

$$G(\kappa_x) = \sum_{n=1}^{N} [\beta_n e^{i\pi y_n/\ell_c}] f_n(\kappa_x) e^{i\kappa_x x_n}. \tag{24}$$

Eq. 24 is immediately seen to be invariant under the simultaneous substitutions

$$\left.\begin{aligned} \beta' &= (-1)^m \beta \\ y' &= y \pm m\ell_c \end{aligned}\right\}, \tag{25}$$

so that the small-angle scattering pattern is unchanged by: (*a*) translating any filament forward or backward along the Y axis by $2\ell_c$, or (*b*) simultaneously changing the sign of a filament while translating it forward or backward along the Y axis by ℓ_c. Accordingly, even if the relative signs of the filaments are known, their relative Y axis locations can only be determined to within multiples of $2\ell_c$, while the relative signs themselves are undeterminable unless the relative Y axis locations of the filaments are already known.

As a result of the foregoing, the relative sign of a filament pair in thick samples cannot be directly determined. For sufficiently thin samples, however, such a determination may still be possible, but in general the sample thickness would need to be less than $\frac{1}{2}\ell_c \simeq 5\ \mu m$. To see the need for such a thin sample consider two filaments, 1 and 2, of initially equal sign, with $y_1 = 0$ and $y_2 = \frac{1}{2}\ell_c$ so that $y_2 - y_1 = +\frac{1}{2}\ell_c$. Now change the sign of, say, filament 2 and translate it backward while translating filament 1 forward so that $y_1' = \frac{1}{2}\ell_c$, $y_2' = 0$, and thus $y_2' - y_1' = -\frac{1}{2}\ell_c$. This sequence of operations is equivalent to changing the sign of filament 2, sliding it backward by ℓ_c, and shifting the origin of coordinates forward by $\frac{1}{2}\ell_c$. But the scattering curve is, of course, always invariant under any translation of the origin, and so the preceding set of operations does not change the scattering curve. We thus conclude that in general the relative sign of an arbitrary pair of filaments cannot be unambiguously determined unless the sample is so thin that translations by $\frac{1}{2}\ell_c \simeq 5\ \mu m$ are not possible.

We have found it impossible to obtain useful samples whose thickness is $<5\ \mu m$, but have been successful in obtaining a small number of good samples $<10\ \mu m$ in thickness. For such samples filament separations of $\Delta y = \ell_c$ are no longer possible, and an unambiguous relative sign determination can be made for those filament pairs for which $\Delta y \simeq 0$, assuming these can be identified. The key to such an identification can be found from computing the SH intensity via Eq. 24 as

$$S_2(\kappa_x) = \sum_{n-1}^{N} \beta_n^2 f_n^2(\kappa_x) + 2 \sum_{\substack{m>n\\-1}}^{N} \sum \beta_m \beta_n f_m(\kappa_x) f_n(\kappa_x) \cdot \cos\left[\kappa_x(\mathrm{x}_m - \mathrm{x}_n) + \kappa_y(y_m - y_n)\right], \quad (26)$$

and noting that if $\Delta y = 0$ then the scattering curve is symmetric in κ_x and thus in scattering angle, while for $\Delta y \neq 0$ an asymmetric scattering curve results.

Results—Filament Signs

Our strategy was to study small-angle scattering from a large number of filament pairs in the thinnest obtainable samples, and to select those curves which were highly symmetric for further analysis. If the sample thickness is T, and the Y axis separations of the filaments are assumed to be random, then the probability $P(|\Delta y|)$ of finding a given value of $|\Delta y|$ is $P(|\Delta y|) = (2/T^2)(T - |\Delta y|)$, and half the filaments can be expected to have $|\Delta y|$ values less than $(1 - \sqrt{2}/2)T = 0.29T$. Accordingly, we could expect to find a significant fraction of symmetric scattering curves in suitably thin samples. Out of some 20 measurements eight yielded highly symmetric scattering curves such as those displayed in Fig. 19 for filament pairs and in Fig. 20 for filament triplets. In every one of these eight cases in which the scattering curves were symmetric, the form of the curve was clearly characteristic of all filaments having the same sign. In no instance were filaments of opposite sign ever found. Based upon random statistics, the probability of such an outcome is <0.5%. Of course, one could argue that our sampling is not truly representative since it involves pairs and triplets of adjacent filaments. Our counter to this is that for one sample we were able to chain the measure-

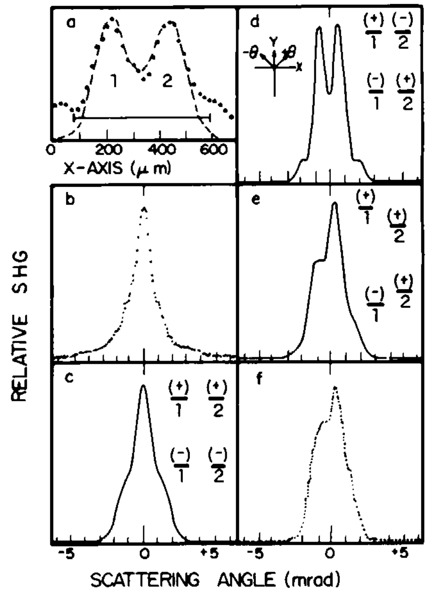

FIGURE 19 Small-angle SH scattering by filament pairs in a very thin sample. The sample thickness was estimated at 7–8 μm based upon the measured retardation and the known birefringence of rat-tail tendon. The coordinate system used and the sign convention for the scattering angle θ are shown in *d*. The laser advances along the $+Y$ direction and the sample lies in the XZ plane with the long tendon axis paralleling the Z axis. (*a*) SH microscope X axis line scan of the filament pair 1, 2. The points (·) are measured data and the curve (---) is a sum of two identical Gaussians of zero Y axis thickness used to model the filaments. The bar (⊢⊣) indicates the region encompassed by the small-angle scattering beam. (*b*) SH scattering curve measured for the filaments of *a*. (*c*) SH scattering curve calculated from Gaussian model assuming that the filaments both have the same sign and the same Y axis coordinates. The calculations include a convolution with the instrumental resolution function and may be directly compared with the experiment in *b*. The labeled, signed bars shown in the figure represent schematically two possible models of the filaments. The good agreement between calculated and measured curves as regards symmetry, zero-angle peak, and overall shape, indicates that the essential features of the model, i.e., filaments with the same sign and some Y axis coordinates, are correct. (*d*) SH scattering curve calculated as in *c* but for filaments of opposite sign. This curve is easily seen to be in total disagreement with the measured data of *b*. (*e*) SH scattering curve calculated as in *c* and *d* but for filaments with Y axis values that differ by $\frac{1}{2}\ell_c = 5\ \mu m$. As discussed in the text, such filament pairs produce asymmetric scattering curves from which the relative signs of the filaments cannot be determined. (*f*) SH scattering measured for a filament pair (not shown) in a thick sample. These data match fairly well the overall shape of *e* and are characteristic of many of the scattering curves obtained with thick samples.

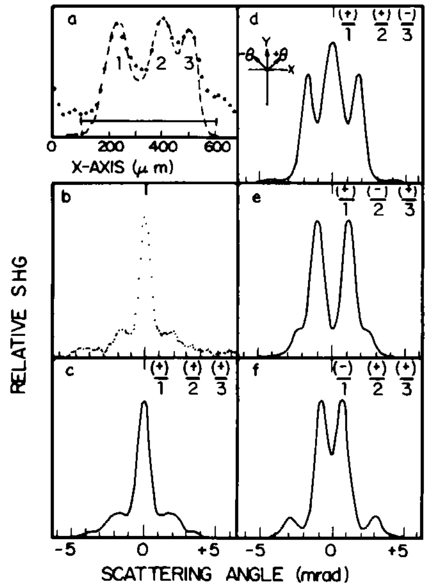

Figure 20 Small-angle SH scattering by filament triplets in a very thin sample. The various symbols, assumptions used, etc. are explained in the caption of Fig. 19. (*a*) SH microscope *X* axis line scan (·), and sum of three Gaussians (---) used to model the filaments. (*b*) SH scattering curve measured for filament triplet of *a*. (*c*) SH scattering curve calculated from Gaussian model under the assumptions that the filaments all have the same sign and same *Y* axis coordinates. The good agreement with the data of (*b*) shows these assumptions to be correct. (*d–f*) Calculated SH scattering as in *c* except for different sign combinations as shown.

ments across the tendon (in all other cases the chain was broken by an intermediate asymmetric data set) and could thus demonstrate for this sample that filaments separated by almost 2 mm still had the same sign. We thus conclude that most, if not all, the filaments in a given tendon are of the same sign.

Results—Filament Locations

Having concluded that essentially all filaments are positive, we proceeded to study small-angle SH scattering by thick samples to determine the *Y* axis locations (surface or bulk) of the filaments. In linear optics a measurement of this sort would not be possible since there κ_y is essentially zero in the small-angle regime, and so the scattering curve would be very nearly independent of the filament *Y* axis locations. In nonlinear optics, however, a single nonzero *Y* axis Fourier component (π/ℓ_c) is available, and since the filaments are thin this single component suffices to fix (modulo $2\ell_c$) the single *Y* axis parameter required for each filament—its *Y* axis location.

To make the measurement we require that three conditions be satisfied. (*a*) The sample region chosen should contain only thin, nonoverlapping filaments. (*b*) The filaments themselves should be reasonably well-separated but spaced sufficiently closely so that a reasonable number fit into the approximately ½ mm-wide beam used for small-angle SH scattering measurements. (*c*) The small-angle pattern should be highly asymmetric and information-rich in the sense that it contains as much fine structure as possible. The crossed-beam SH microscope was used to find a sample region that met the first two conditions. This region was then scanned systematically (under computer control) and a large number of small-angle patterns were generated, each over a limited angular range near the origin. The most promising looking of these was then rescanned over a larger angular range, and the resultant data subjected to exhaustive analysis. In Fig. 21 we illustrate the selection procedure, and in Fig. 22 we display the complete small-angle scattering pattern chosen.

In analyzing this pattern we assumed a simple Gaussian shape for the *X* axis filament profiles and further assumed that all filaments were very thin and that Eq. 23 was valid. Each of the eight filaments was thus describd by four parameters: amplitude, width, *X* axis position and *Y* axis

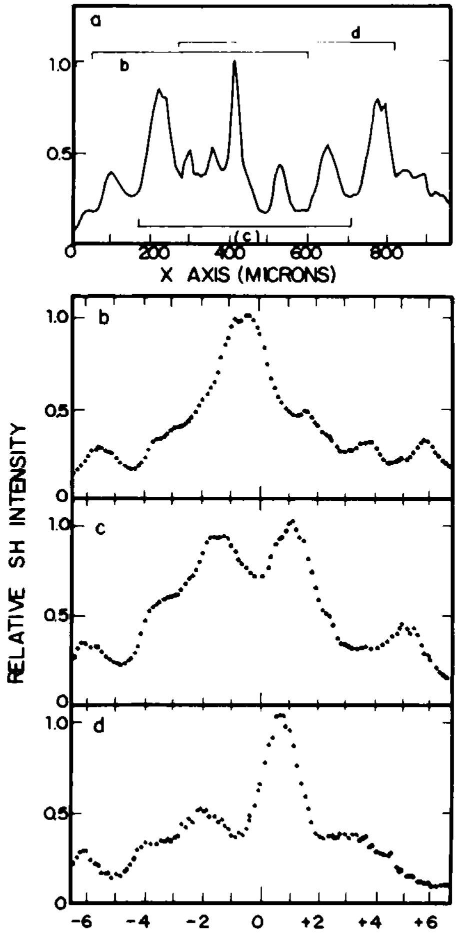

Figure 21 Small-angle SH scattering by selected groups of filaments. (*a*) SH microscope *X* axis line scan. The bars (⊢⊣) labeled *b, c*, and *d* delineate the filament groups whose small-angle scattering curves are shown in *b, c*, and *d*. These data are part of an extended set used to select a filament group with a rich, multipeak SH scattering curve that could be analyzed to yield the filament *Y* axis locations. The filament set chosen was *c*.

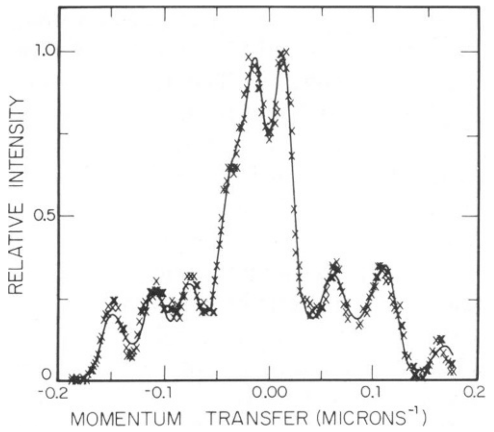

FIGURE 22 SH scattering curve vs. momentum transfer for filament group (*c*) of Fig. 21. The solid line (—) is calculated from a full-matrix least-squares fit to the data (x) using the Gaussian model which is described fully in the text and is illustrated schematically in Fig. 23.

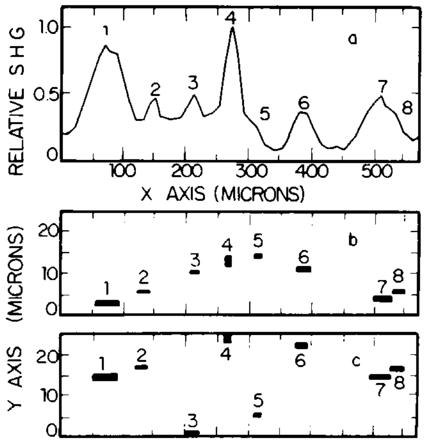

FIGURE 23 (*a*) SH microscope *X* axis line scan of filament set used to determine filament *Y* axis positions. (*b–c*) Two possible models of filaments, both of which give the exact same SH scattering curve (Fig. 22) as explained in the text. The widths of the bars are the widths of the Gaussians in the model used to fit the scattering data, while the thickness of the bars are proportional to the amplitudes of the Gaussians, the thicknesses of the filaments themselves being assumed to be zero. The model in *b* is just about the most compact one possible whereas that in *c* is the most open. In both of these, and in all other possible models, the filaments appear to permeate the tendon volume in an apparently random fashion.

location. Initial estimates of the first three parameters were easily obtained from the SH microscope images, although it was recognized that in some instances the scanning spot size probably exceeded the true filament widths and so the assumed amplitudes and widths would need to be adjusted later. We further recognized that slight adjustments might also be required in the *X* axis positions since the microscope and small-angle scattering beams undoubtedly sampled slightly different regions.

The *Y* axis locations, however, presented a unique problem since no prior information was available for these. Our solution to obtaining initial *Y* axis estimates was to first compute the Patterson sine and cosine functions of the scattering curve and then to identify the various positive and negative peaks with appropriate sets of pairs of filaments using the interfilament spacing as given by the SH microscope. The sign of each peak in the Patterson sine/cosine function depends upon the sine/cosine of κ_y times the *Y* axis separation of the corresponding filament pair. Thus, each filament could be assigned to a given quadrant, of size $\frac{1}{2}\ell_c \simeq 5$ μm, while a more detailed consideration of intensities permitted a further refinement such that initial *Y* axis location could be estimated to ~2 μm.

Using these initial values a full matrix least-squares refinement was performed, with convergence being rapid and smooth, and final parameters being satisfyingly close to the initial estimates. Included in the fitting procedure was a convolution with the instrumental resolution function. The goodness of fit to the scattering data, as measured in the usual way (33), gave a pleasing *R* value of 0.05, half of which was estimated as being due to experimental noise and the remainder to small systematic deviations, engendered by the simplicity of the Gaussian model.

In Fig. 23 we display on an expanded scale both the SH microscope data and schematics of two possible filament arrangements. As already indicated, any filament can be translated forward or backward along the *Y* axis by $2\ell_c$ without affecting the scattering pattern, and so many alternative arrangements are possible. All of these can be obtained by reproducing the pattern of, say, Fig. 23 *a* a number of times along the *Y* axis with a spacing of $2\ell_c$, and then sliding a window equal in height to the sample thickness (≃25 μm) along this repetitive pattern. All arrangements in which each filament shows up once and only once in the window are physically possible ones fully consistent with the scattering data. When this procedure is performed no special filament patterns (such as all near-surface) emerge, and so we conclude that the filaments permeate the bulk of the tendon in an essentially random fashion.

DISCUSSION

The two most pressing questions regarding the polar structures are: what are they made of and what do they do? Since no real information of any sort is available regarding function, unbridled speculation is possible but not necessarily fruitful. A determination of the major molecular constituents of the polar structures would, on the other hand, represent a major advance which could also be expected to provide important clues regarding function.

Are the polar structures composed of collagen? Since collagen is so abundant in tendon it would appear to be a particularly convenient source of polar material, especially if the function of the polar structures was to serve as purely physical transducers such as strain gages, accelerometers, or temperature sensors. We have already presented circumstantial evidence that the polar structures are not composed of collagen fibrils, evidence which is suggestive but by no means definitive. Here we argue that the collagen triple helix is actually not strongly polar and is thus not a good candidate for the construction of strongly polar structures. In Fig. 24 we present a view of a typical turn of the α_1 chain of collagen using atomic coordinates for the "standard structure" as given by Ramachandran (34). As may be noted from this figure, the strongly polar C═O and N—H bonds all tend to lie very nearly normal to the chain axis and so make a negligible contribution to the net dipole moment. The various C—H bonds also tend to be more-or-less normal to the chain axis, and since these bonds are anyway only weakly polar they contribute little to the net moment. The geometry of the αC—N and C′—N bonds is such that extensive cancellation of their dipole moments also occurs. Indeed, if these two bond moments were equal their net contribution would be quite small. An estimate of effective atomic charges for peptides (35) suggests, however, that the C′—N bond dipole moment is ~25% greater than the αC—N moment, so that a small but nonnegligible net moment persists. But this is virtually the only significant contribution to the net dipole moment of collagen since the various side chains are not only highly mobile (36–38), but can also be expected to exhibit a large internal cancellation. For example, for the sequence Gly-Pro-Hyp we again find that $\langle \theta^z_{C=O} \rangle = 92.4°$ and $\langle \theta^z_{C-N-C} \rangle = 92.4°$. The possible contribution of bound water is a complex topic which requires special consideration. Experimentally we find, however, that there is no large difference in fibril SH intensities between wet and dry samples, so that we do not believe water plays an important role in the overall polarity of collagen. We note that the absolute nonlinear susceptibility of the collagen fibril (12) is an order of magnitude less than is usual for strongly polar crystals (22), a finding which also tends to support our conclusion that collagen is not highly polar and that the polar structures of connective tissue are likely to be composed of other substances.

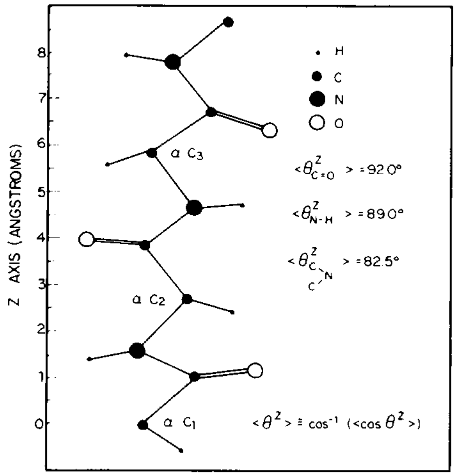

FIGURE 24 Schematic model of three representative residues that make up approximately one turn of the α_1 helix of type I collagen. The α-carbon side chains are not shown. The figure is not a true projection but is drawn to correctly reproduce the angles θ^Z that the various polar bonds make relative to the chain (Z-) axis, i.e., the Z axis coordinates and the bond lengths are all correct. As may be seen from the figure, and as is also the case for the sequence Gly, Pro, Hyp, the net directions of each of the strongly polar bond types is nearly normal to the chain axis, leading to the conclusion that the collagen molecule is not strongly polar.

Visualization of the polar structures by SHG should permit their isolation for study by a wide variety of techniques. The surface patches, in particular, would appear to be easily accessible candidates, and could conveniently be investigated by scanning and transmission electron microscopy. Chemical, enzymatic, and thermal degradation studies as well as use of immunofluorescence and other specific labelling methods should also prove highly informative. Accordingly, it may soon prove possible to resolve the 20-yr old mystery of connective tissue polarity.

Received for publication 3 March 1986.

REFERENCES

1. Fukada, E., and I. Yasuda. 1964. Piezoelectric effects in collagen. *Jpn. J. Appl. Phys.* 3:117–121.
2. Nye, J. F. 1964. Physical Properties of Crystals. Oxford Univ. Press, London.
3. Ueda, H., and E. Fukada. 1971. Piezoelectricity in myosin and actin. *Jpn. J. Appl. Phys.* 10:1650–1651.
4. Fukada, E., and Y. Ando. 1972. Piezoelectricity in oriented DNA films. *J. Polymer Sci. A2.* 10:565–567.
5. Fukada, E. 1974. Piezoelectric properties of biological macromolecules. *Advan. Biophys.* 6:121–155.
6. Lang, S. B. 1966. Pyroelectric effect in bone and tendon. *Nature (Lond.).* 212:704–705.
7. Athenstaedt, H. 1970. Permanent electric polarization and pyroelectric behavior of collageneous structures and nervous tissue in man and other vertebrates. *Nature (Lond.).* 228:830–834.
8. Athenstaedt, H. 1974. Electric properties of vertebrates. *Ann. NY Acad. Sci.* 238:68–93.
9. Liboff, A. R., and M. Furst. 1974. Pyroelectric effect in collageneous structures. *Ann. NY Acad. Sci.* 238:26–34.
10. Traub, W., and K. A. Piez. 1971. The chemistry and structure of collagen. *Adv. Protein Chem.* 25:243–352.
11. Anderson, J. C., and C. Eriksson. 1968. Electrical properties of wet collagen. *Nature (Lond.).* 218:166–168.
12. Roth, S., and I. Freund. 1981. Optical second-harmonic scattering in rat-tail tendon. *Biopolymers.* 20:1271–1290.
13. Roth, S. 1981. Second Harmonic Light Scattering from Macromolecules. Univ. Microfilms Int., Ann Arbor.
14. Sheppard, C. J. R., J. N. Gannaway, R. Kompfner, and D. Walsh. 1977. The scanning harmonic optical microscope. *IEEE Trans.* QE13:100D.
15. Gannaway, J. N., and C. J. R. Sheppard. 1978. Second harmonic imaging in the scanning optical microscope. *Opt. Quant. Electronics.* 10:435–439.
16. Sheppard, C. J. R., and R. Kompfner. 1978. Resonant scanning optical microscope. *Appl. Opt.* 17:2879–2882.
17. Sheppard, C. J. R. 1982. Applications of scanning optical microscopy. *Proc. Soc. Photo-Opt. Instrum. Eng.* 368:88–95.
18. Parry, D. A. D., and A. S. Craig. 1977. Quantitative electron microscope observations of the collagen fibrils in rat-tail tendon. *Biopolymers.* 16:1015–1031.

19. Bloembergen, N. and P. S. Pershan. 1962. Light waves at the boundary of nonlinear media. *Phys. Rev.* 128:606–622.

20. Armstrong, J. A., N. Bloembergen, J. Ducuing, and P. S. Pershan. 1962. Interactions between light waves in a nonlinear dielectric. *Phys. Rev.* 127:1918–1939.

21. Bersohn, R., Y. H. Pao, and H. L. Frisch. 1966. Double-quantum light scattering by molecules. *J. Chem. Phys.* 45:3184–3198.

22. Yariv, A. 1971. Introduction to Optical Electronics. Ch. 8. Holt, Rinehart, and Winston, New York.

23. Cyvin, S. J., J. E. Rauch, and J. C. Decius. 1965. Theory of hyper-Raman effects (nonlinear inelastic light scattering): selection rules and depolarization ratios for the second-order polarizability. *J. Chem. Phys.* 43:4083–4095.

24. Kleinman, D. A. 1962. Nonlinear dielectric polarization in optical media. *Phys. Rev.* 126:1977–1979.

25. Roth, S., and I. Freund. 1982. Second harmonic generation and orientational order in connective tissue: a mosaic model for fibril orientational ordering in rat-tail tendon. *J. Appl. Cryst.* 15:72–78.

26. Panter, P. F. 1965. Modulation, Noise and Spectral Analysis. Ch. 4. McGraw-Hill, Inc., New York.

27. Roth, S., and I. Freund. 1981. Optical second harmonic generation in collagen: evidence for a macroscopic polarity in rat-tail tendon. Structural Aspects of Recognition and Assembly in Biological Macromolecules. M. Balaban, editor. Balaban Intl Sci. Services. Rehovot, Israel. 447–462.

28. Diamant, J., A. Keller, E. Baer, M. Litt, and R. G. C. Arridge. 1972. Collagen; ultrastructure and its relation to mechanical properties as a function of ageing. *Proc. R. Soc. London. B. Biol. Sci.* 180:293–315.

29. Cusack, S., and A. Miller. 1979. Determination of the elastic constants of collagen by Brillouin light scattering. *J. Mol. Biol.* 135:39–51.

30. Meek, K. M., J. A. Chapman, and R. A. Hardcastle. 1979. The staining pattern of collagen fibrils: improved correlation with sequence data. *J. Biol. Chem.* 254:10,710–10,714.

31. Born, M., and E. Wolf. 1959. Principles of Optics. Ch. 8. Macmillan Publishing Co., New York.

32. Koechner, W. 1976. Solid State Laser Engineering. Springer-Verlag, New York.

33. Hamilton, W. C. 1974. Tests of the R-factor ratio. International Tables for X-Ray Crystallography. Vol. IV, Sect. 4.2. J. A. Ibers and W. C. Hamilton, editors. Kynoch Press, Birmingham, England.

34. Ramachandran, G. N. 1967. Structure of collagen at the molecular level. Treatise on Collagen. Vol. I, Chap. 3. G. N. Ramachandran, editor. Academic Press, Inc., New York.

35. Weiner, S. J., P. A. Kollman, D. A. Case, U. Chandra Singh, C. Ghio, G. Alagona, S. Profeta, Jr., and P. Weiner. 1984. A new force field for molecular mechanical simulation of nucleic acids and proteins. *J. Am. Chem. Soc.* 106:765–784.

36. Jelinski, L. W., and D. A. Torchia. 1980. Investigation of labeled amino acid side-chain motion in collagen using ^{13}C nuclear magnetic resonance. *J. Mol. Biol.* 138:255–272.

37. Jelinski, L. W., C. E. Sullivan, and D. A. Torchia. 1980. ^{2}H NMR study of molecular motion in collagen fibrils. *Nature (Lond.).* 284:531–534.

38. Jelinski, L. W. and D. A. Torchia. 1979. $^{13}C/^{1}H$ high power double magnetic resonance investigation of collagen backbone motion in fibrils and in solution. *J. Mol. Biol.* 133:45–65.